Formulation and validation of a reduced order model of 2D materials exhibiting a two-phase microstructure as applied to graphene oxide

Ivano Benedetti [a,b,1], Hoang Nguyen [c,1], Rafael A. Soler-Crespo [c,1], Wei Gao [a,d], Lily Mao [f], Arman Ghasemi [d], Jianguo Wen [e], SonBinh Nguyen [f], Horacio D. Espinosa [a,c,*]

[a] Department of Mechanical Engineering, Northwestern University, 2145 Sheridan Road, Evanston, IL 60208-3111, USA
[b] Dipartimento di Ingegneria Civile, Ambientale, Aerospaziale e dei Materiali, Università degli Studi di Palermo, Viale delle Scienze, Edificio 8, 90128, Palermo, Italy
[c] Theoretical and Applied Mechanics Program, Northwestern University, 2145 Sheridan Road, Evanston, IL 60208-3111, USA
[d] Department of Mechanical Engineering, University of Texas at San Antonio, San Antonio, TX 78249, USA
[e] Center for Nanoscale Materials, Argonne National Laboratory, Lemont, IL 60439, USA
[f] Department of Chemistry, Northwestern University, 2145 Sheridan Road, Evanston, IL 60208-3111, USA

ARTICLE INFO

ABSTRACT

Novel 2D materials, *e.g.*, graphene oxide (GO), are attractive building blocks in the design of advanced materials due to their reactive chemistry, which can enhance interfacial interactions while providing good in-plane mechanical properties. Recent studies have hypothesized that the randomly distributed two-phase microstructure of GO, which arises due to its oxidized chemistry, leads to differences in nano- *vs* meso–scale mechanical responses. However, this effect has not been carefully studied using molecular dynamics due to computational limitations. Herein, a continuum mechanics model, formulated based on density functional based tight binding (DFTB) constitutive results for GO nano-flakes, is establish for capturing the effect of oxidation patterns on the material mechanical properties. GO is idealized as a continuum heterogeneous two-phase material, where the mechanical response of each phase, graphitic and oxidized, is informed from DFTB simulations. A finite element implementation of the model is validated via MD simulations and then used to investigate the existence of GO representative volume elements (RVE). We find that for the studied GO, an RVE behavior arises for monolayer sizes in excess to 40 nm. Moreover, we reveal that the response of monolayers with two main different functional chemistries, epoxide-rich and hydroxyl–rich, present distinct differences in mechanical behavior. In addition, we explored the role of defect density in GO, and validate the applicability of the model to larger length scales by predicting membrane deflection behavior, in close agreement with previous experimental and theoretical observations. As such the work presents a reduced order modeling framework applicable in the study of mechanical properties and deformation mechanisms in 2D multiphase materials.

© 2017 Elsevier Ltd. All rights reserved.

---

* Corresponding author.
  E-mail address: espinosa@northwestern.edu (H.D. Espinosa).
[1] These authors contributed equally to this work.

1. Introduction

The design of the next generation of advanced engineering materials, whose behavior fully synergizes different building blocks across different length scales, stands to benefit from the integration of tailorable building blocks. Two-dimensional (2D) materials have been identified, for these engineering applications, as particularly promising candidates given their exceptional mechanical properties and tailorable surface-to-volume ratios. For instance graphene oxide (GO), an oxidized variant of graphene composed of oxidized domains (∼3-5 nm in diameter) interspersed within a graphitic matrix, is composed of hydroxyl and epoxide chemistries that provide unique mechanochemical properties amenable to engineering applications (Erickson et al., 2010). Furthermore, GO has been shown to possess tunable microstructure and mechanical properties (Soler-Crespo et al., 2016), which have led to significant research interest. Indeed, GO has been employed by the scientific community for energy devices (Xu et al., 2010; Kuila et al., 2013), water filtration membranes (Jang et al., 2015), structural materials (Medhekar et al., 2010; Compton et al., 2012; Xu et al., 2009; Beese et al., 2014) and molecular sensors (Robinson et al., 2008; Dua et al., 2010; Ryoo et al., 2013) due to its unique combination of facile fabrication pathways, modest mechanical properties and chemical reactivity (Wei et al., 2015; Cao et al., 2015; Paci et al., 2007). From an engineering point of view, this degree of tunability creates a materials space that must be closely inspected before GO is widely adopted in applications of interest.

As previously alluded to, a manifestation of the complex materials space that GO inhabits is its complex microstructure, which is largely determined by its chemical composition. For instance, recent transmission electron microscopy studies have revealed that GO is composed of stochastically distributed, island-like patterns that cover a graphitic backbone. Recent experimental and theoretical studies have focused on determining intrinsic and local properties of GO due to limitations in the employed techniques (Soler-Crespo et al., 2016; Wei et al., 2015; Cao et al., 2015; Erickson et al., 2010). However, it is unclear if the presence of this microstructure changes materials performance beyond what is predicted from atomistic calculations, and if such observations would impact the viability of the material in structural applications. For example, GO has been shown to transition from a brittle to quasi-brittle material as its relative epoxide composition increases (Soler-Crespo et al., 2016), which leads to dramatic increases in strain to failure in atomistic calculations. The extension of such phenomena beyond the nanoscale, however, has not yet been assessed.

The verification of such observations necessitates the development of particular investigative tools that are not presently available within the scientific community investigating this material. For instance, recent coarse grained (CG) molecular dynamics (MD) models allow simulation of relatively large GO monolayers (Meng et al., 2017), but they cannot probe the manifestation of such phenomena at the nanoscale due to limitations in computational power. Equivalently, the design of experiments that can directly probe the tensile properties of meso–scale specimens remains a continuing challenge to researchers. For this reason, the development of theoretical tools based on continuum theory that can probe meso–scale systems is critical. By having access to such tools, investigative efforts into the mechanics of GO at larger scales would be possible. Only by probing the materials at these length scales would researchers be able to determine transitions in mechanical behavior that can guide materials design processes.

In this work, we develop a continuum model for GO membranes based on a heterogeneous, two-phase approach. Density functional based-tight binding (DFTB) simulations are performed to determine the fundamental behavior of graphitic and oxidized regions with varying chemical composition, which then guide the development of energetically-consistent constitutive laws. The derived model is validated by comparing the predicted mechanical behavior of large GO sheets to MD simulations. Then, the model is utilized to probe the existence of RVEs in GO and to assess the influence of microstructure and defects in the mechanical performance of GO. Finally, we show the predictive power of the model by performing membrane deflection simulations that predict the role of defect density and fracture process on previously reported experimental findings (Wei et al., 2015; Cao et al., 2015).

This paper is organized as follows: Section 2 details the development of algorithms to generate meaningful GO microstructures and the constitutive laws for each of the phases in the model. Section 3 discusses the numerical implementation of the model, and the application of a crack band model to enhance the mesh objectivity of the performed analysis. The model is validated against MD calculations of large GO sheets in Section 4. Then, in Sections 5–7, the model is applied in a variety of fundamental studies to assess the existence of RVEs and the influence of microstructure in the mechanics of GO. Finally, Section 8 provides concluding remarks and an outlook into the use of the developed framework.

2. Model development

In the continuum framework developed herein, a GO monolayer is modeled as a heterogeneous, two-phase membrane in which highly disordered, oxidized regions are interspersed over a regular graphitic matrix. The continuum properties for each of the two phases, namely the graphitic and oxidized regions, are assigned by fitting stress-strain behavior obtained from DFTB simulations of 2×2 nm^2 representative nano-flakes subjected to uniaxial and equibiaxial strain tensile loading. A continuum damage model, developed in this work, is used to represent the behavior of the oxidized regions, while graphitic areas are modeled adopting a nonlinear-elastic continuum model (Wei et al., 2009; Wei and Kysar, 2012) enriched with a failure criterion. Failure strains for the graphitic and oxidized phases are identified from DFTB simulations, and translated into the continuum model in terms of strain failure criteria. The role of defects in the mechanical behavior of GO is also investigated by introducing damaged regions within each of the two modeled phases and will be discussed in a later section.
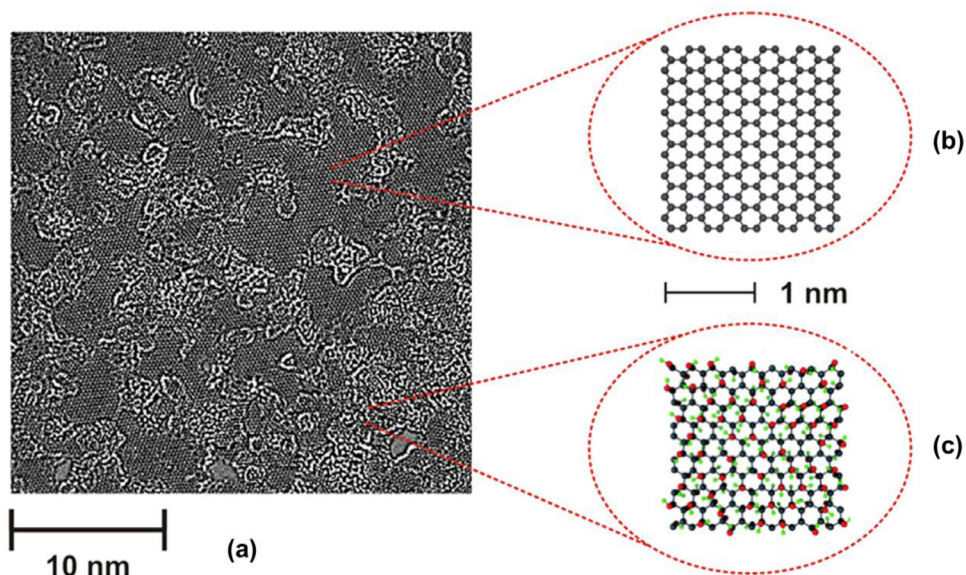
Fig. 1. (a) High-resolution transmission electron microscope image of a graphene oxide monolayer consisting of (b) graphitic regions with a crystalline, hexagonal microstructure and (c) oxidized regions with a highly disordered microstructure. In the atomistic models, gray, red and green beads correspond to carbon, oxygen, and hydrogen atoms, respectively. (For interpretation of the references to color in this figure legend, the reader is referred to the web version of this article.)

2.1. Morphology generation

As previously shown in the literature, GO refers to a class of materials whose microstructure and chemical composition depends on the adopted synthesis route (Erickson et al., 2010; Soler-Crespo et al., 2016). Recently, based on high-resolution transmission electron microscopy (HRTEM), GO has been shown to possess a highly inhomogeneous structure in which crystalline graphitic regions, disordered regions (*i.e.,* oxidized domains), and voids are simultaneously present (Fig. 1). The relative area percentage of graphitic and oxidized regions, as well as voids in the matrix, depends on the fabrication method. For instance, Erickson et al. (2010) reported HRTEM observations for GO monolayers with 16%, 82% and 2% of the area corresponding to graphitic regions, oxidized regions and voids, respectively. When thermally treated, reduced graphene oxide (rGO) becomes predominantly graphitic (70% area coverage), at the cost of an increase in hole density (5% area coverage). Given the variability of its microstructure, from the continuum mechanics modeling point of view, GO can be considered as a random, heterogeneous, two-phase material.

On the basis of the above observations, a random sequential adsorption algorithm (Feder, 1980) is used to generate artificial microstructures employed in the computational analysis of GO to investigate the existence of a representative volume element. The algorithm consists of: (i) scattering a set of N seed points randomly, starting from a uniform distribution, within a rectangular box representing the GO domain to be analyzed, while requiring a minimum distance d between points; (ii) associating a circular region of radius R to each seed, without requirements on the superposition of contiguous regions between seeds; (iii) considering the region inside each circle as oxidized, while the remaining regions are considered graphitic. The algorithm represents numerically an oxidation reaction, starting at random oxidation nuclei and proceeding isotropically for a limited distance, before energetic considerations disrupt the kinetics of the reaction at a distance R from the oxidation nuclei. Different ratios between the oxidized and overall patch areas can be obtained varying the total number of seeds N for a fixed combination of R and d. In the present study, we observed that fixing $N = 160$, $R = 1$ nm and $d = 0.5$ nm generated reasonable microstructures for a 30×30 nm^2 monolayer (Fig. 2). The algorithm was used to generate multiple random, heterogeneous microstructures which were analyzed in the continuum mechanics framework to inquire the existence of RVEs in GO.

2.2. Modeling of graphitic regions

The continuum model adopted for the description of the graphitic regions in GO assumes that the lack of local oxidation leaves the graphitic backbone unaltered. In this light, it is appropriate to describe the local behavior in graphitic regions using available continuum models for graphene. Wei et al. (2009); Wei and Kysar (2012) and Xu et al. (2012) used density functional theory to develop energetically consistent, continuum constitutive laws for pristine graphene. These studies predict a non-linear elastic behavior with significant anisotropy at high strains. Furthermore, Wei and Kysar (2012) validated the developed constitutive response in light of the agreement between measured and simulated membrane deflection exper-
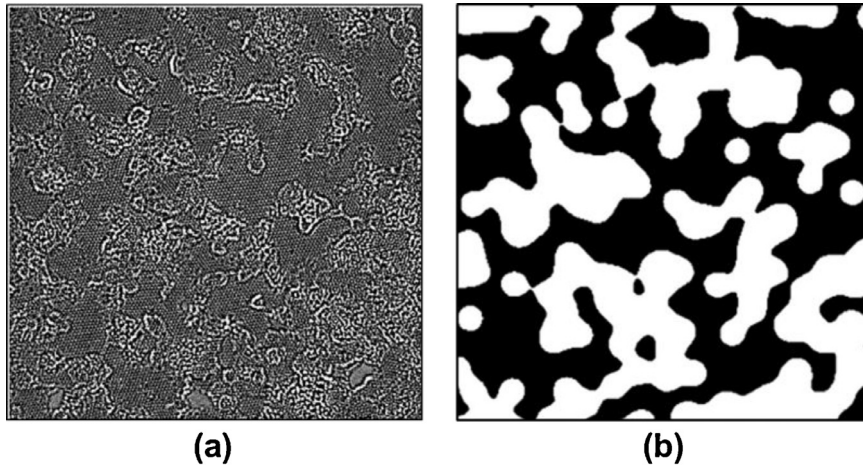
Fig. 2. Generation of artificial morphologies of graphene oxide (GO) membranes. (a) High-resolution transmission electron microscope image of a 30 nm × 30 nm region in a GO monolayer. (b) Artificial morphology obtained with the proposed algorithm ($N = 160$, $r = 1$ nm, $d = 0.5$ nm). Oxidized regions are colored white, while graphitic regions are colored black. (For interpretation of the references to color in this figure legend, the reader is referred to the web version of this article.)

iments on circular, free-standing monolayer graphene. Similarly, Lu and Huang (2009) also developed a similar constitutive model for monolayer graphene based on molecular mechanics simulation and the second generation of reactive empirical bond order potential (REBO).

The constitutive model for graphene is based on the existence of a nonlinear-elastic potential Ψ, which has the form of a Taylor expansion

$$\Psi(\boldsymbol{\eta}) = \frac{1}{2!}C_{ij}\eta_i\eta_j + \frac{1}{3!}C_{ijk}\eta_i\eta_j\eta_k + \frac{1}{4!}C_{ijkl}\eta_i\eta_j\eta_k\eta_l + \dots \tag{1}$$

such that

$$\Sigma_i = \frac{\partial \Psi}{\partial \eta_i} = C_{ij}\eta_j + \frac{1}{2!}C_{ijk}\eta_j\eta_k + \frac{1}{3!}C_{ijkl}\eta_j\eta_k\eta_l \dots \tag{2}$$

where η_i and Σ_i are components of the Green-Lagrange strain tensor and the work-conjugate second Piola-Kirchhoff stress tensor, respectively, while C_{ij}, C_{ijk} and C_{ijkl} represent second, third and fourth order elasticity constants, respectively. In the previous expressions, subscripts have been expressed in Voigt notation, so that the indices *i, j, k* and *l* vary between 1 and 6, in integer increments. Under this notation, second, third and fourth order elasticity constants correspond precisely to components of the fourth, sixth and eight order elasticity tensors, when represented in indicial notation. The number of independent elastic constants to be determined for each elasticity tensor, for a general deformation state, can be easily evaluated from the number of subscripts for the specific tensor. However, this number of independent elastic constants is greatly reduced if the symmetries of the graphene lattice are taken into account, and if only the in-plane strain components are considered. For this case, Wei et al. (2009) determined the number of independent constants for the elasticity tensors up to the fifth order expansion under Voigt notation (2, 3, 4 and 5 independent constants for the fourth, sixth, eighth and tenth order elasticity tensors when represented in indicial notation) to capture the anisotropy found in DFT simulations of graphene.

In this work, the continuum model is built starting from DFTB simulations. We find that an energetically consistent continuum representation of graphene is obtained by retaining up to the eighth order elasticity tensor (in indicial notation) in the nonlinear-elastic potential Ψ, with a total of 9 independent constants. Fig. 3 shows the components of stress along the zigzag and armchair directions when graphene is loaded under uniaxial strain along the zigzag and armchair directions, or when equibiaxial strain is applied. To achieve consistency between stress measures for GO and graphene, we utilize GO's thickness ($t_0 = 0.75$ nm) (Rezania et al., 2014) as a reference value for the analysis. The use of a representative thickness normalizes the behavior of oxidized and graphitic regions. This ensures that the curves of 2D stress $\boldsymbol{\Sigma_{2D}}$ and strain $\boldsymbol{\eta}$ are consistent between different thickness values. Furthermore, because plane stress conditions are reasonable, no stress is expected to manifest in the out of plane direction. Similarly, the employed Poisson's ratio should be contextualized as 2D rather than 3D. It is important to note that the out-of-plane thicknesses play a key role when considering multilayer structures, and can be assigned on the basis of measured inter-layer distances as commonly done in the literature. Herein, unless specified otherwise, when stresses of the form Σ_L^U are provided, the *U* index represents the direction along which displacement is controlled, while the *L* index represents the stress measure direction. Continuum curves are obtained by least squares fitting the DFTB data, with the nonlinear-elastic representation of stress in Eq. (2), yielding the values of the
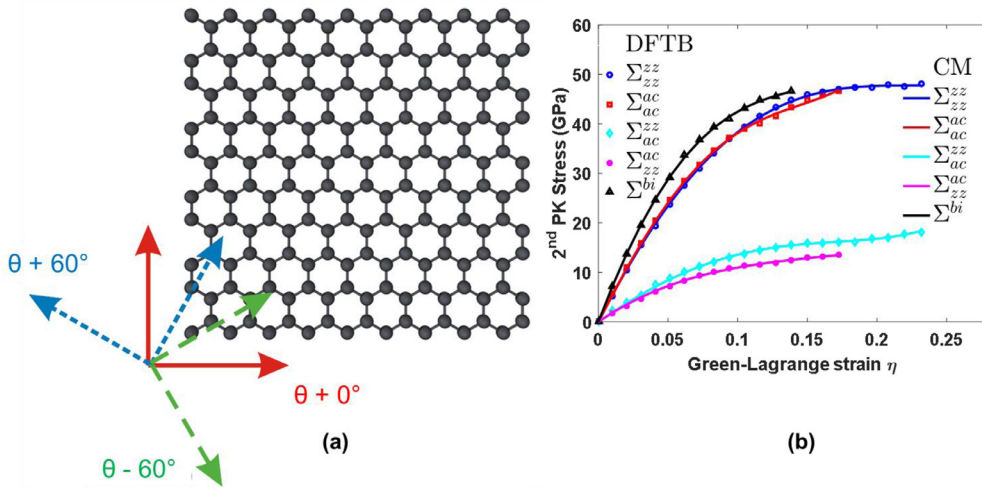
Fig. 3. (a) 2 nm × 2 nm model used for density functional based-tight binding (DFTB) simulations of graphene. Three mechanically equivalent orthogonal reference systems ($\theta + 0°$, $\theta + 60°$ and $\theta - 60°$) are shown. (b) Stress-strain curves for the DFTB simulated graphene. Here, Σ_{ac}^{zz} represents the armchair (ac) component of the 2nd Piola-Kirchhoff stress tensor when a uniaxial strain along the zigzag (zz) direction is applied; the other symbols have analogous meaning. The markers correspond to points obtained through DFTB simulations, while the continuum curves express the nonlinear-elastic continuum model.

Table 1
Nonlinear-elastic coefficients. Units in N m^{-1}.

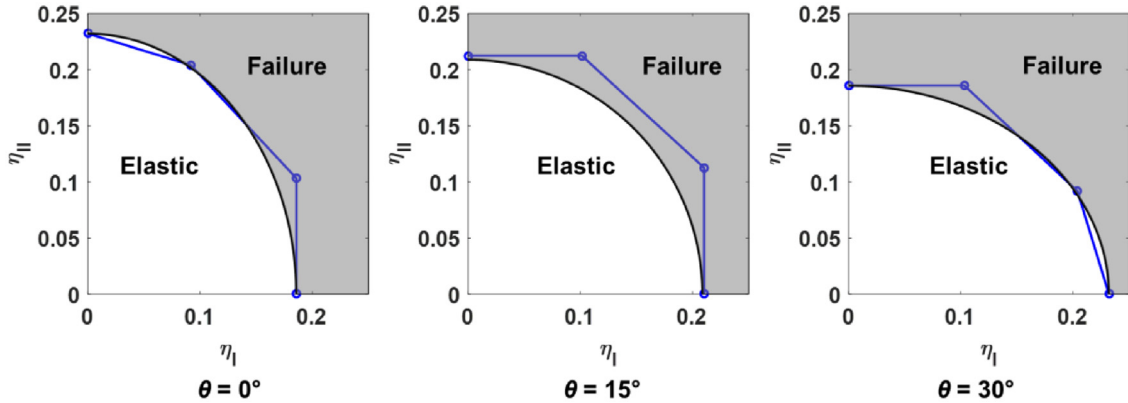| SOECs	TOECs	FOECs
$C_{11} = 435.61$	$C_{111} = -3473.60$	$C_{1111} = 13,628.66$
$C_{12} = 139.48$	$C_{112} = -912.430$	$C_{1112} = 2396.27$
	$C_{222} = -3098.32$	$C_{1122} = 5069.61$
		$C_{2222} = 6110.84$

Fig. 4. In-plane principal strain-based failure criterion for the graphene continuum model. Eq. (3) is illustrated for three example reference systems, each at a different angle θ. Blue curves represent the real failure surface due to phonon instability (Marianetti and Yevick, 2010), while black curves represent the approximate surface predicted by the failure model. (For interpretation of the references to color in this figure legend, the reader is referred to the web version of this article.)

independent constants reported in Table 1. For further details about the general expressions of in-plane stress components in graphene, see Wei et al. (2009).

The DFTB simulations also provided values of failure strains for graphene, which showed a clear dependence on the loading orientation with respect to the lattice. Moreover, Marianetti and Yevick (2010) indicated that graphene displays a failure mechanism corresponding to soft mode instabilities, which reduces the failure strains of graphene in certain loading conditions, in comparison with the failure strains due to elastic instabilities associated with sp^2 C–C bonds. This result in different failure surfaces for various loading orientations (see Fig. 4). Based on this phenomenon, and since the simulations are performed under displacement control, a strain-based criterion is proposed. In particular, in the model, failure occurs
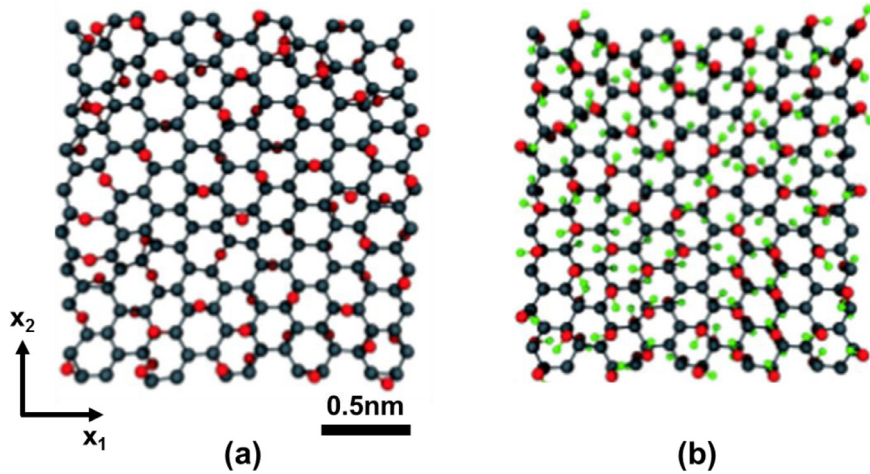
Fig. 5. Representative and oxidized GO monolayers used in the DFTB simulations. The monolayers have an (a) epoxide-rich and (b) hydroxyl–rich chemistry. Gray, red and green beads represent carbon, oxygen and hydrogen atoms, respectively. (For interpretation of the references to color in this figure legend, the reader is referred to the web version of this article.)

according to the failure surface ξ given by:

$$\xi(\boldsymbol{\eta}) = \sqrt{(\eta_I/A)^2 + (\eta_{II}/B)^2} = 1, \qquad (3)$$

where η_I and η_{II} are the components of in-plane principal strains along the first and second principal directions, respectively, and A and B are parameters that will change as functions of θ, where θ is the angle between the armchair and the first principal direction (Fig. 3). It is important to realize that A and B in Eq. (3) must be periodic with respect to a 60° angle due to the crystalline structure of graphene. Therefore, these parameters can be written as trigonometric functions of θ. The shape of the failure surface will change as θ changes, and the failure criterion may be satisfied in one case of θ, but not in the others, and this is a sufficient condition to trigger failure. Fig. 4 presents three cases corresponding to $\theta = 0°$, $\theta = 15°$ and $\theta = 30°$. The functions for A and B are given by $A = 0.20895 + 0.02315 \cos(6\theta)$ and $B = 0.20895 - 0.02315 \cos(6\theta)$.

2.3. Oxidized regions and a thermodynamic framework for the continuum damage model of GO

GO can be oxidized by epoxide or hydroxyl functional groups, as shown in Fig. 5. Analogous to the procedure employed for graphene in Section 2.2, the behavior of oxidized configurations has been simulated using DFTB (Wei et al., 2015; Soler-Crespo et al., 2016), and the resulting behavior guides the formulation of a continuum model for the oxidized regions, consistent with the strategy used for graphitic regions. The control volume employed for each representative configuration is $2 \times 2 \times 0.75$ nm^3, and the armchair direction of the material is aligned with the x_1 reference direction, while the x_3 direction is aligned with the control volume thickness. The monolayers are deformed applying uniaxial strain along the zigzag or armchair direction, or equibiaxial strain, and the stress in each loading direction is computed according to the virial theorem. Since the microstructure of GO is stochastic, different oxidized microstructures with identical chemical composition were generated, utilizing a configurational bias Monte Carlo-based algorithm shown to assimilate the kinetics and chemistry that determine the formation of GO, to probe the role of structure on the mechanical response of GO (Paci et al., 2007; Wei et al., 2015). The local behavior of an oxidized region, in the proposed modeling scheme, is fully contained within one of GO's oxidized islands. For this reason, the representative GO nano-flakes are modeled by considering the maximum attainable level of oxidation for the chemistries under consideration (Soler-Crespo et al., 2016; Meng et al., 2017). These maximum attainable oxidation levels are 80% for epoxide rich monolayers and 72% for hydroxyl rich monolayers.

The stress-strain curves obtained for 8 epoxide-rich GO monolayers, under different loading conditions, are shown in Fig. 6. The second Piola-Kirchhoff stress and Green-Lagrange strain are reported for work-conjugate consistency, and to follow the notation employed for the graphitic matrix. Thick blue and red lines in Fig. 6a represent third-order least square approximations for Σ_{zz}^{zz} and Σ_{ac}^{ac} stress components, *i.e.* stress measured in directions coincident with uniaxial strain loading directions. During our DFTB simulations, it is possible to observe a slight anisotropy between the stress-strain response in zigzag and armchair directions (Fig. 6a), which reduces during equibiaxial strain loading (Fig. 6b). This anisotropy is not significant as the blue, red and black curves are almost indistinguishable in Fig. 6, and for this reason, and to guide continuum modeling, an average isotropic behavior is determined for epoxide-rich GO nano-flakes.

To determine this average isotropic behavior of epoxide-rich GO monolayers, we consider both Σ_{zz}^{zz} and Σ_{ac}^{ac} stress components as representative of a generic stress component Σ_x^x, conjugated with the loading uniaxial strain η_x along the generic loading direction x. Similarly, both Σ_{zz}^{ac} and Σ_{ac}^{zz} stress components serve as representative samples of a generic (transverse)
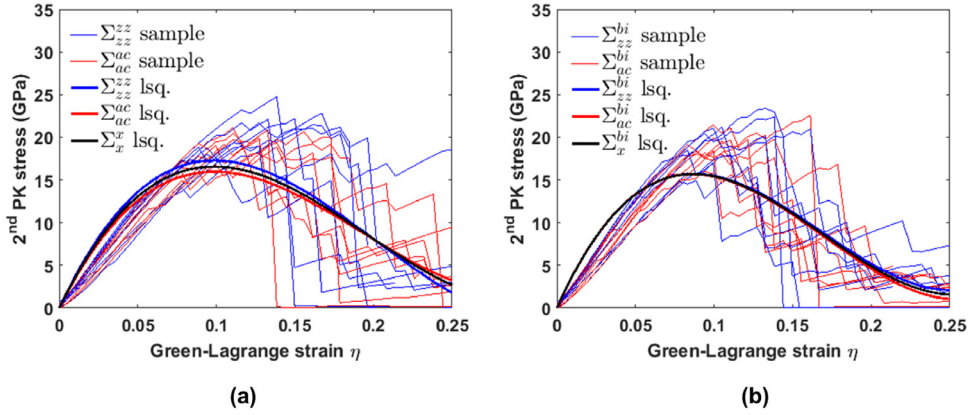
Fig. 6. Stress-strain curves for representative, epoxide-rich GO monolayers, subjected to (a) uniaxial strain loading, and (b) equibiaxial strain loading. Thin lines represent results from DFTB calculations for individual monolayers (with 8 tested samples), while thick lines are obtained from a third-order least square fitting of obtained stress-strain results. (For interpretation of the references to color in this figure legend, the reader is referred to the web version of this article.)
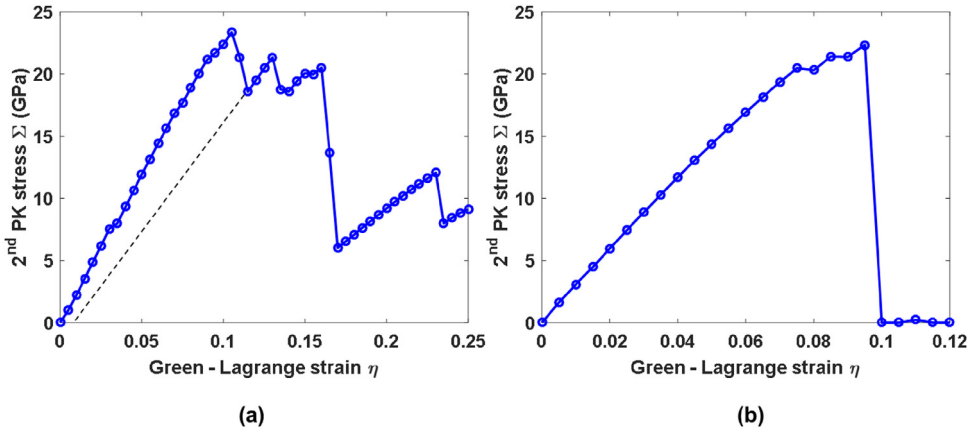

Fig. 7. Representative stress-strain curves which show (a) progressive, stepwise stiffness degradation of an epoxide-rich GO monolayer (unloading represented by a dashed, black line) and (b) abrupt failure of hydroxyl–rich GO monolayers.

stress component Σ_y^x along the generic direction *y*, perpendicular with respect to the uniaxial loading direction *x*. Such a directionally average behavior is represented by the thick black lines in Fig. 6, which serve as an indirect basis for the development of the proposed continuum model. The same conclusion has also been reached for hydroxyl–rich GO.

To gain insight into the mechano-chemical behavior of oxidized regions and formulate a physically based continuum model of their mechanical response, it is necessary to analyze more closely the response of each representative specimen. Uniaxial strain tension tests along the armchair direction, Σ_{ac}^x, for epoxide-rich and hydroxyl–rich GO monolayers are shown in Fig. 7a and b, respectively. Discrete stress drops in stress-strain behavior, due to bond breaking events, reduce the apparent stiffness of epoxide-rich GO monolayers, as captured in Fig. 7a. Indeed, previous DFT- and DFTB-based atomistic studies have shown bond-breaking events in graphitic and oxidized regions lead to changes in mechanical behavior.

In the analysis of epoxide-rich GO (Fig. 7a), the damage process is divided into two stages: micro-damage evolution and localization. The former corresponds to the transformation of a small amount of epoxide functional groups into ether chemistries, due to the rupture of C–C bonds participating in these chemical bonds, as discussed elsewhere (Dreyer et al., 2010; Soler-Crespo et al., 2016). This transformation plays a key role in dissipating energy through mechano-chemically activated chemical reactions that visually manifest in stress-strain responses and make GO act as a quasi-brittle material. Notably, this procedure assimilates small-scale bridging of toughened ceramic. On the other hand, the latter corresponds to the accumulation of epoxide-to-ether transformations, and the eventual failure of ether groups by strain localization. Unloading after damage has accumulated in epoxide-rich GO reveals the presence of residual strain (*i.e.,* the unloading strain at zero stress is not zero); however, this value is small enough so we consider the material to fully unload. In contrast to epoxide-rich GO, Fig. 7b shows the brittle behavior associated to hydroxyl–rich GO, as a consequence of C–C bond stretching to a threshold value followed by an abrupt failure. In agreement with previous literature, hydroxyl–rich GO is treated as a perfectly brittle material (Soler-Crespo et al., 2016).

It is interesting to observe that DFTB results can be approximated using the relation $\Sigma_x^x = E(\phi, \eta_x) \cdot \eta_x$ and assuming a phenomenological progressive stepwise stiffness degradation of the form (analogous to a sawtooth damage model)

$$E(\phi, \eta_x) = E_0(\phi) - \sum_k \Delta E_k \cdot H(\eta_x - \bar{\eta}_k) \tag{4}$$

where $E_0(\phi)$ is the stiffness of a pristine GO nano-flake with oxidation level ϕ (Soler-Crespo et al., 2016), and ΔE_k are discrete stiffness drops activated at specific deformations, *i.e.*, strain thresholds $\bar{\eta}_k$. The agreement between the stress-strain curves obtained by DFTB calculations and the curve obtained by employing Eq. (4), after selecting a suitable set of parameters, suggests that the introduction of some damage parameter for modeling the progressive stiffness degradation and eventual failure of functionalized patches is necessary to track local damage evolution in GO monolayers. However, even though Eq. (4) sheds light on the nanomechanics of damage in GO monolayers, the use of analogous functional forms at a continuum level triggers numerical issues due to the stepwise representation of stiffness degradation. By employing concepts explored in modeling continuum damage mechanics (Melro et al., 2013; Kachanov and Krajcinovic, 1987), we introduce a thermodynamically consistent damage model for oxidized regions in GOs.

First, we define the strain energy density function for a material point in a plane stress condition as:

$$\Psi(d, \boldsymbol{\eta}) = \frac{1}{2} \frac{E (1-d)^m}{1-\nu^2(1-d)^{2m}} (\eta_1^2 + \eta_2^2) + \frac{E\nu (1-d)^{2m}}{1-\nu^2(1-d)^{2m}} \eta_1 \eta_2 + G (1-d)^m \eta_6^2 \tag{5}$$

where E, G and ν are the Young's modulus, shear modulus and Poisson's ratio of pristine GO at a certain degree of oxidation ϕ, respectively. Here, $d[\boldsymbol{\eta}] \in [0, 1]$ is a parameter expressing the progressive accumulation of irreversible damage, which depends on the history of local strain state $\boldsymbol{\eta}$. The power m is chosen to match the failure surface of GO under different loading conditions. The specific functional form of Ψ is selected using the DFTB results for representative GO monolayers. This functional form must be able to describe hydroxyl– and epoxide-rich GO monolayers, and fully characterize the behavior of GO in each case. To define this functional form, we assume that GO monolayers: (i) behave isotropically prior to any damage and orthotropically after the onset of damage, and (ii) have different failure strains under uniaxial and equibiaxial loading. To ensure the irreversibility of the damage process, the rate of change of the strain energy must be less than or equal to the external applied stresses by satisfying

$$\boldsymbol{\Sigma} : \dot{\boldsymbol{\eta}} - \dot{\Psi}(d, \boldsymbol{\eta}) \geq 0 \tag{6}$$

Inequality (6) is required to ensure the positive dissipation of energy in any mechanical process. Expanding this equation and applying the chain rule yields

$$\left(\boldsymbol{\Sigma} - \frac{\partial \Psi}{\partial \boldsymbol{\eta}} \right) : \dot{\boldsymbol{\eta}} - \frac{\partial \Psi}{\partial d} \dot{d} \geq 0 \tag{7}$$

To satisfy Inequality (7) in any loading path requires that the term inside the parenthesis be equal to zero. This implies that the stresses must be calculated by taking the derivative of the strain energy with respect to the strain tensor (or vector in Voigt notation) so that

$$\boldsymbol{\Sigma} = \frac{\partial \Psi}{\partial \boldsymbol{\eta}} = \boldsymbol{D}(d) : \boldsymbol{\eta}; \boldsymbol{D} = E \begin{bmatrix} \frac{(1-d)^m}{1-\nu^2(1-d)^{2m}} & \frac{\nu(1-d)^{2m}}{1-\nu^2(1-d)^{2m}} & 0 \\ \frac{\nu(1-d)^{2m}}{1-\nu^2(1-d)^{2m}} & \frac{(1-d)^m}{1-\nu^2(1-d)^{2m}} & 0 \\ 0 & 0 & \frac{(1-d)^m}{1+\nu} \end{bmatrix} \tag{8}$$

where $\boldsymbol{D}$ represents the stiffness matrix at a certain level of damage. Based on the form of the stiffness matrix, the compliance tensor $\boldsymbol{C} = \boldsymbol{D}^{-1}$ is

$$\boldsymbol{C} = \frac{1}{E} \begin{bmatrix} \frac{1}{(1-d)^m} & -\nu & 0 \\ -\nu & \frac{1}{(1-d)^m} & 0 \\ 0 & 0 & \frac{1+\nu}{(1-d)^m} \end{bmatrix} \tag{9}$$

As a result of the definition of stress, the irreversibility condition given by Inequality (7) reduces to $-(\partial \Psi / \partial d) \dot{d} \geq 0$. The thermodynamic force is therefore defined as $Y = -(\partial \Psi / \partial d)$, which is work-conjugate to the damage coefficient d. The damage onset and damage accumulation processes depend on the definition of Y, which is taken as:

$$Y = \frac{Em[(1-d)^{m-1} + \nu^2(1-d)^{3m-1}]}{2[1-\nu^2(1-d)^{2m}]^2} (\eta_1^2 + \eta_2^2) + \frac{2mE\nu (1-d)^{2m-1}}{[1-\nu^2(1-d)^{2m}]^2} \eta_1 \eta_2 + Gm (1-d)^{m-1} \eta_6^2 \tag{10}$$

As a consequence of Eq. (10), when $Y \geq 0$, the condition given by Eq. (7) further reduces to $\dot{d} \geq 0$, in agreement with the second law of thermodynamics. The definition of the secant stiffness matrix in Eq. (8) allows calculations of stresses in the material based on its current strain and damage progression. However, a condition that specifies the onset of damage must be defined. Herein, we choose to specify the onset of damage using
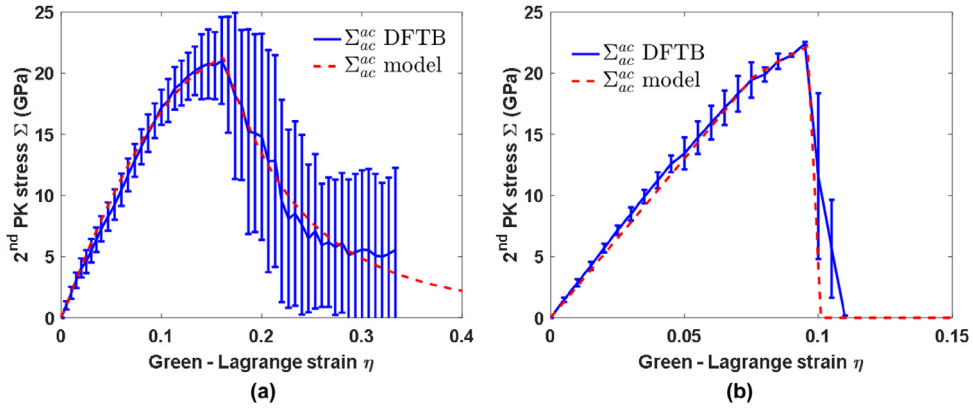
$$F^d = \sqrt{Y} - \kappa(d) \leq 0 \tag{11}$$

Fig. 8. Comparison of DFTB stress strain curves and predicted stress-strain behavior in uniaxial tension test of (a) epoxide-rich GO and (b) hydroxyl–rich GO. Solid blue curves and error bars correspond to the average and one standard-deviation error for the DFTB measurement. The red, dashed lines correspond to the model predictions. (For interpretation of the references to color in this figure legend, the reader is referred to the web version of this article.)

where F^d represents a damage potential or function and κ is an internal function related to the damage variable. This internal function will in turn be equal to κ_0 when damage starts to accumulate. Notably, in the elastic regime or during unloading process, the condition $F^d < 0$ applies. However, once damage is activated, the guiding condition instead becomes $F^d = 0$. Similar to elasto-plastic materials, Kuhn-Tucker conditions (Hanson, 1981) can also be applied to separate loading and unloading process by considering

$$\dot{d} \geq 0, F^d \leq 0, \dot{d}F^d = 0 \tag{12}$$

If the internal variable is solely dependent on the damage variable, and the loading function is defined in terms of the strain tensor, the constitutive model can be explicitly integrated. However, stress must be calculated based on the current level of damage and strains, and damage in turn depends on the strains of a local material point, so an elastic predictor – damage corrector algorithm and the Newton–Raphson iterative scheme must be applied.

The final element for the damage model is the expression of κ as a function of the damage variable, d. The type of function utilized should also be versatile, so it may be implemented for different GO chemical compositions. The function is separated into two components, following the two stage damage process described earlier. The model is given by

$$\kappa = \begin{cases} \kappa_0 + \kappa_f (1 - \exp(-\alpha d)), d \leq d_0 \\ \kappa_d \sqrt{1 - \beta(d - d_0)}, d > d_0 \end{cases} \tag{13}$$

where κ_0 is the damage initiation threshold, and κ_f and κ_d are parameters controlling the magnitude of damage. To ensure κ is a C_0 continuous function, we select $\kappa_d = \kappa_0 + \kappa_f (1 - \exp(-\alpha d_0))$. Here, d_0 is the damage threshold that distinguishes between the two damage processes. α and β are shape parameters that control the rate of change of the function. It is important to note that the influence of β on regularizing energy dissipation as a function of element size is later described, and used to tune the softening response based on the employed crack band model. For hydroxyl–rich GO, due to the absence of epoxide groups, the corresponding value of d_0 will be close to zero so that the damage-evolution portion is limited while its associated β value will be large to characterize the steep drop in the stress- strain curve. On the contrary, these parameters will be finite and manifest themselves in a broader range of prescribed strains for epoxide-rich GO. One constraint on β in this function is that the value must not be larger than $1/(d - d_0)$ so the term under the square root is positive. The ability of the damage model to fully predict the uniaxial tensile behavior of GO monolayers is shown in Fig. 8.

In order to fully capture the behavior of GO under different loading paths, a failure surface is visualized in the plane of principal strains (Fig. 9a). Three distinctive regions can be described: an elasticity region, a region where material damage progresses (through strengthening and subsequently softening), and a failure region. The material response will fall within one of these regions depending on the current strain state $\boldsymbol{\eta}$ and the value of the damage variable d; in general loading, unloading and reloading stages can be precisely predicted by this model. Fig. 9b shows that the derived model slightly underestimates the failure strain under equibiaxial tension. The observed discrepancy stems from the formulation of the thermodynamic force and the shape of the failure surface, which are constructed based on an energy-consistent framework. The strain energy density function (5) is chosen to match the behavior of Σ_x^x and Σ_y^x in uniaxial experiments, while equibiaxial tension is used to validate the function behavior. We note that the discrepancy in equibiaxial behavior can be compensated by an overestimation of uniaxial tensile behavior. However, due to the island-like distribution of the oxidized area, none of the elements is loaded locally in pure equibiaxial tension, even when the specimen undergoes macroscopic equibiaxial tension.

It should be noted that, in the present model, grain boundaries are not considered, and their effect on the mechanical behavior of graphene can be found elsewhere (Jhon et al., 2012). In principle, such effects could be described by multiple-
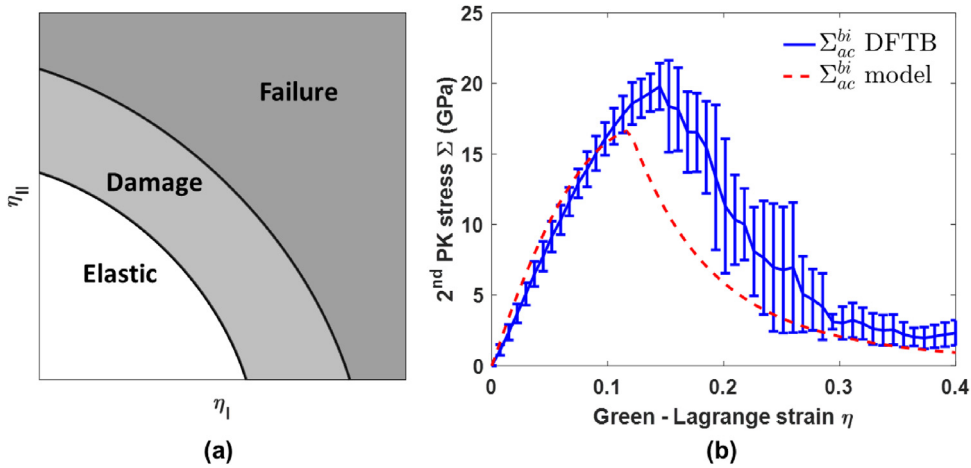
Fig. 9. (a) Typical failure surface predicted by the proposed model. Elastic, damage and failure regions are identified. (b) Comparison of the stress strain curves of epoxide-rich GO monolayers under equibiaxial strain between DFTB and as predicted by the derived model.

phase models, in which each graphitic region is assigned an armchair orientation relative to the x-axis. In such case, inter-granular resistances and interactions between grains should be suitably considered and are outside the scope of this paper.

3. Finite element analysis implementation

The continuum representations developed for graphitic and oxidized regions in GO were implemented in the finite element software ABAQUS 6.14 to study continuum GO monolayers represented as heterogeneous two-phase structures. The implementation of a user material subroutine to implement the previously described models, and the technique adopted to mitigate spurious mesh dependencies which arise when modeling failure, are described in this section.

3.1. User material subroutine

The developed models were implemented in the commercial finite element software ABAQUS/Explicit (Abaqus, 2014). Within ABAQUS, the material model has been implemented by defining a VUMAT user material subroutine. Stress tensor updates at each integration point and time increment are handled by the VUMAT subroutine. ABAQUS passes certain variables into the VUMAT, such as the deformation gradients F_i and F_f, where the subscripts i and f denote quantities at the beginning and the end of the time increment, respectively. Such quantities must be suitably used to update the stress components with respect to the proposed framework.

In this work, and due to the heterogeneous microstructure of GO monolayers, continuum models for graphitic and oxidized GO regions have been implemented, and the selection of the appropriate updating equations is handled by employing a state variable within VUMAT which expresses the local oxidation level ϕ at the integration point under consideration. Depending on the local value of ϕ, the appropriate constitutive laws, either Eqs. (2) and (3), or Eqs. (8) through (13), are used to update stress components. In the VUMAT implementation a second state variable stores the irreversible damage level for the integration points belonging to the oxidized regions, while a third state variable is required by ABAQUS to enable element failure and deletion. The VUMAT has been implemented for membrane elements under the assumption of in-plane deformations and zero out-of-plane bending stiffness; such an assumption also holds for deformations exhibiting out-of-plane rotations, as long as the elastic strain energy induced by bending is small with respect to that induced by in-plane deformations. In the VUMAT, the armchair direction of the graphene substrate is aligned with the local x_1 axis, the zigzag direction is aligned with the local x_2 axis and the local x_3 axis is normal to the membrane plane. Since 3D membrane elements may undergo out-of-plane displacements, care must be taken to ensure the frame invariance of the constitutive relationships. ABAQUS achieves frame objectivity expressing the constitutive laws in local coordinate systems, instantaneously rotating with the material at each integration point; more specifically the constitutive laws are defined in a co-rotational framework based on the Jaumann stress rate (ABAQUS, 2014).

For this work, we will utilize the prefixes micro- and macro- in reference to computed local fields and homogenized values over the volume, respectively. Herein, the micro stress update within the VUMAT subroutine is achieved as follows. For each integration point:

(i) The frame-invariant right stretch tensor at the end of the time increment, U_f, which is readily available within the VUMAT, is used to compute the Green-Lagrange strain tensor η_f according to

$$\eta_f = \frac{1}{2}\left(U_f^2 - I\right) \tag{14}$$

where I is the identity tensor.

(ii) The state variable that tracks oxidation level is assessed and the appropriate stress update subroutine, either for graphitic or oxidized GO regions, is invoked passing η_f as an input. A non-zero state variable for the oxidation level is considered as an oxidized GO region.

(iii) For graphitic regions, stresses are updated according to $\Sigma = \Sigma(\eta_f)$ with the nonlinear-elastic model given by Eqs. (2) and (3). For oxidized regions, the state variable d_i is extracted and used to update the value of the damage function and the loading function associated with the current strain state η_f. If the material point is unloading or undamaged then $F^d < 0$ and the damage value from previous step is conserved. When $F^d = 0$, a damage corrector algorithm is activated. Eventually, Eqs. (8) through (13) are computed for η_f and used to update stress components. Damage variables are updated at the end of the time increment.

(iv) Since ABAQUS requires Cauchy stress components as the outputs from the VUMAT, the computed second Piola–Kirchhoff stress components Σ_f are converted into σ_f using the standard relation:

$$\sigma_f = J_f^{-1} F_f \Sigma_f F_f^T \tag{15}$$

Where F_f is the deformation gradient at the end of the time interval and J_f is the determinant of the deformation gradient, *i.e.,* the deformation Jacobian.

3.2. Ensuring mesh objectivity

A simple and often used strategy for representing local material failure within FE codes consists in the removal of elements whose integration points have reached a failure threshold. This procedure, known as element deletion, can be seen as an abrupt discrete softening process, in which the stiffness of the failing elements is suddenly reduced to zero, so some elements lose their load bearing capability upon fulfillment of a certain failure condition. Unfortunately, this modeling strategy is known to induce strain localization and spurious mesh sensitivity, compromising the objectivity of the FE analysis. In this regard, the mesh objectivity of the developed finite element implementation is crucial to accurately identify GO RVEs.

Various strategies have been proposed in the literature to overcome mesh sensitivity and improve mesh objectivity (Bazant and Planas, 1997). The most sophisticated approaches resort to non-local formulations, in which local measures of strain and stresses are replaced by non-local counterparts, obtained through suitable integral averaging of the local fields based on the definition of a material characteristic length, which smear damage over material regions independently from the mesh (Pijaudier-Cabot and Bažant, 1987). The crack band model (Bažant and Oh, 1983), which assumes that the failure process zone can be represented by a damaged finite element zone that has the width of one element, is a more adaptable framework to ensure mesh objectivity. In this framework, the dissipated fracture energy is regularized by considering the material fracture toughness and the characteristic length h_e^c of the finite elements. This method has been shown to be appropriate for the treatment of large structures undergoing complex damage mechanisms, and achieves global response objectivity.

The crack band model avoids energetic inconsistencies by taking into account the mesh size and endowing each finite element with a material constitutive law supplemented with a post-failure softening behavior, whose features depend on the material's fracture toughness and on the characteristic length of the element itself, h_e. This approach prevents that energy dissipation at failure becomes arbitrarily small upon mesh refinement. To illustrate the technique, consider the uniaxial stress-strain curve shown in Fig. 10a, where DFTB simulations (*e.g.,* the curve shown with a black line) yield a specific material response, and subsequent colored lines correspond to arbitrary material softening responses. A generic finite element obeying this material law will fail at η_f and absorb, at failure, an amount of energy per unit area corresponding to $(W_1 + W_2)h_e$, where h_e is aforementioned characteristic length of the element. Physically h_e should be taken in the loading direction or perpendicular to the crack direction. The crack band model then requires that:

$$(W_1 + W_2)h_e = G \tag{16}$$

where G is the critical material energy release rate, *i.e.* the fracture energy. Since W_2 is the energy density tuned by modifying the softening part of the stress-strain curve, there is mathematical flexibility in the choice of the element's size. In particular, given a certain material fracture energy, h_e can be increased to reduce W_2. However, this process is limited by the fact that, beyond a certain threshold element size h_e^*, identified by the condition $W_2 = 0$, the material law should exhibit constitutive snap-back to fulfill the condition in Eq. (16), which would be unphysical. A critical element length size is then identified by the relationship

$$h_e^* = \frac{G}{W_1} \tag{17}$$

To ensure physically meaningful mesh consistency, no element in the mesh should have its size h_e larger than h_e^*. Moreover, at each integration point, the material law should be dependent on the size of the element to which it belongs to. If possible, the element size h_e should be selected considering inherent material features, which was described by Bazant and Planas (1997), and no element should be smaller than the length so selected h_e^c.

Herein, the critical element sizes for elements in graphitic and oxidized regions, and the parameters defining the crack band softening, are computed in Appendix A by assuming a thickness $t_0 = 0.75$ nm, which leads to a fracture energy G– of
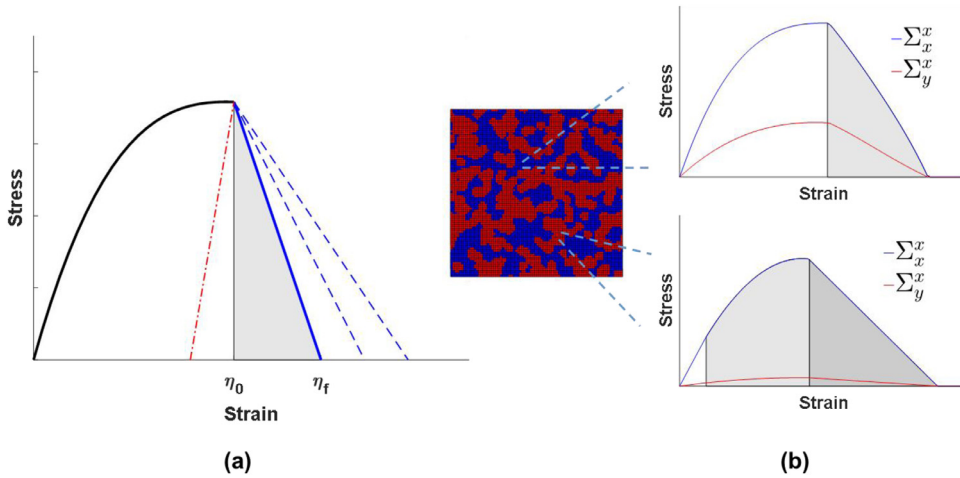
Fig. 10. (a) Example of material law with tunable softening. The response plotted by solid lines corresponds to stress-strain behavior extracted from DFTB computations. Softening responses (blue dashed curves) can be tuned using the measured fracture energy and element size h_e. To avoid constitutive snap-back (red dashed curve), a maximum element length size h_e^* must be identified. (b) Finite element scheme for the analysis of heterogeneous GO membranes. Different material laws are assigned to graphitic (blue) and oxidized (red) regions. The local constitutive laws are tuned with crack band softening, whose extent depend on the assumed characteristic element length. (For interpretation of the references to color in this figure legend, the reader is referred to the web version of this article.)

6.11 J/m^2 for epoxide-rich GO and 2.5 J/m^2 for hydroxyl–rich GO. These values are comparable with previous reports on GO's fracture energy (Meng et al., 2017), and only slightly lower than experimental and theoretical measurements of graphene's fracture energy when its intrinsic fracture energy is scaled to account for thickness differences (G–16 J/m^2 at $t_0 = 0.34$ nm, which leads to G–7 J/m^2 at GO's thickness) (Zhang et al., 2014). Using the constitutive laws developed for graphitic and oxidized regions in GO, critical element sizes $h_{graphitic}^* = 0.78$ nm, $h_{epoxide}^* = 3.20$ nm and $h_{hydroxyl}^* = 2.01$ nm are computed. Due to these observations, a characteristic finite element length $h_e = 0.50$ nm $< h_{graphitic}^*$ has been selected for the computations, which does not exceed the critical values given above, and allows resolving the oxidized microstructure of GO with adequate resolution in terms of microstructural features and mesh objectivity constraints. Specifically, Fig. 10 shows a schematic of the FE model implemented for the analysis of heterogeneous GO membranes.

4. Validation of FEM model with MD simulations

Herein, FEM constitutive laws were built based on DFTB calculations, which have been shown to capture reasonably well the mechanical behavior of GO (Soler-Crespo et al., 2016). However, due to microstructural effects at length scales that DFTB cannot capture, it became critical to obtain verification of the FEA model at larger length scales. To this end, we conducted molecular dynamics (MD) simulations on a 20×20 nm^2 GO monolayer, with a morphology that assimilated that used in a separate FEA calculation. We intended to validate the FEA model by directly comparing the macro stress-strain and failure behavior of the same GO monolayer in both approaches (Fig. 11 and Fig. 12). For the performed calculations, the GO sheets contained an oxidation level of 78% with a 4:1 epoxide to hydroxyl functional group ratio. MD simulations employed the ReaxFF force field (Van Duin et al., 2001), a reactive force field that has been parametrized for predictions with hydrocarbons and graphene oxide-based systems (Chenoweth et al., 2008). For the atomistic model, the location of functional groups are randomly distributed inside predefined oxidized domains that match the FEM morphology. The GO sheets are deformed by applying uniaxial strain on the armchair direction at 300 K, with a Noose-Hoover thermostat, within the NVT ensemble.

In Fig. 11, the virial stress of GO as a function of strain as obtained from MD simulations is compared with the stress–strain curve obtained from FEM calculations. As shown, the ultimate stress and strain from FEM is comparable with MD simulations. Notably, the entropic effect due to rippling, at finite temperature, is responsible for the initial concave curvature at small strains, resulting in non-zero stresses at zero strain, as previously discussed elsewhere (Gao and Huang, 2014). Since out-of-plane wrinkles in GO are not considered in the model here presented, such entropic stresses and negative Poisson's ratio, due to out-of-plane effects (Wan et al., 2017), do not emerge. By imposing uniaxial stretching, the warped GO is flattened before in-plane atomic bonds bear load. This process is indicated by the initial part of the MD stress-strain curve in Fig. 11, and is not captured in FEM as we assume the sheet is initially taut. Therefore, in order to ensure the two results are comparable, we shifted the MD curve to coincide with the FEM prediction, at the inflection point of the MD curve. The stiffness measured in FEM ($E = 271$ GPa) shows a good agreement with MD ($E = 250$ GPa) values. The development of damage prior to failure is also well captured, as manifested by the similar stiffness degradation between the two models. Notably, the agreement between our FEM and MD results provides a validation of the elastic behavior of our model for larger scales,
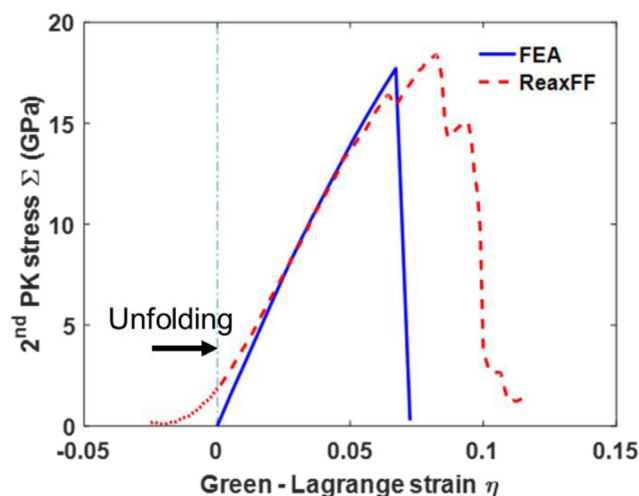
Fig. 11. Stress-strain comparison between FEM and MD. MD results have been shifted to account for initial sheet stretching to remove intrinsic wrinkling due to GO chemistry.
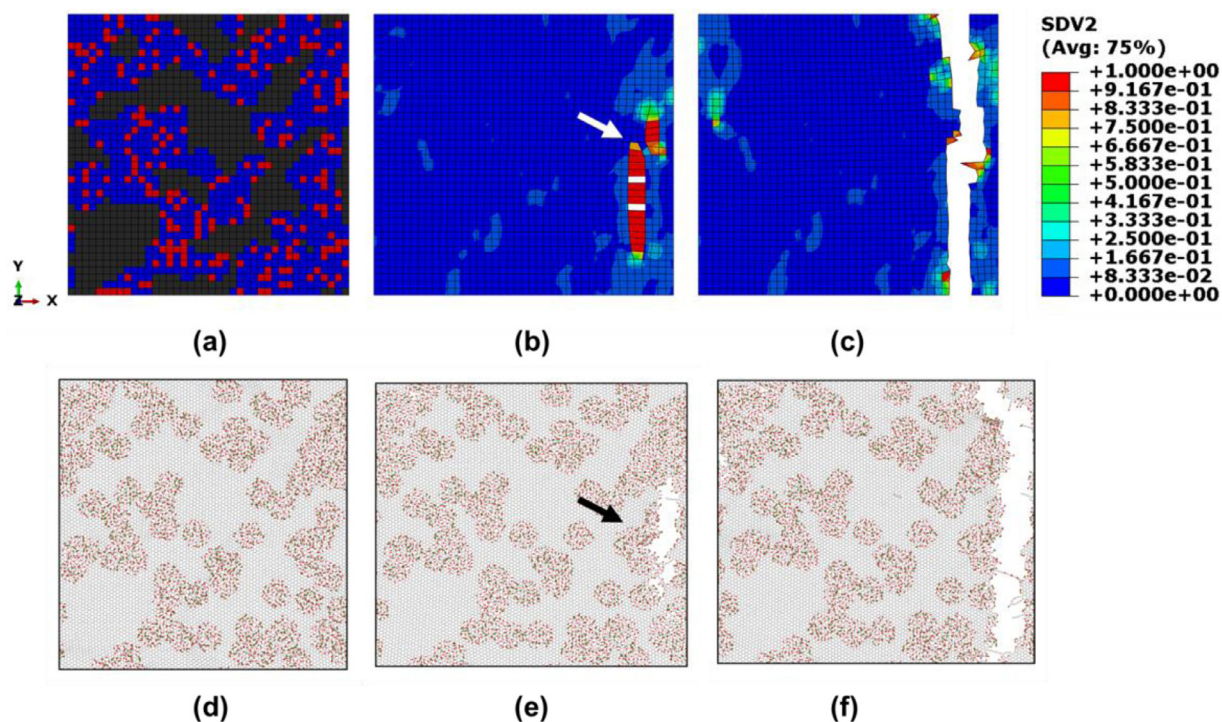

Fig. 12. (a) Oxidized area distribution of FE simulation, gray, blue and red colors indicate graphitic, epoxide and hydroxyl–rich regions respectively; (b-c) Damage initiation (white arrow) and propagation of FE model at strains (b) $\eta = 6.8\%$ and (c) $\eta = 7.0\%$, respectively.; (d) Oxidized area distribution in MD simulations; gray, red and green colors indicate carbon, oxygen and hydrogen atoms, respectively (e-f) Damage initiation (black arrow) and propagation of MD model at (e) $\eta = 7.2\%$ and (f) $\eta = 7.4\%$, respectively. (For interpretation of the references to color in this figure legend, the reader is referred to the web version of this article.)

and confirms the accuracy of DFTB in predicting the local elastic properties of GO sheets. To further confirm the validity of our FEM models, we compared the evolution of damage and failure mechanisms in FEM and MD.

The failure process in our FEM simulations is captured in Fig. 12b–c, while the evolution of damage in the atomistic simulations is shown in Fig. 12e–f. We start by noting the oxidation degree and pattern (arising from the two phases), and the ratio of functional groups are kept the same in both FEA and MD simulations. The only difference is the specific spatial distribution of the groups because they are generated randomly in each case. Unsurprisingly, damage in both of the MD and FEA simulations initiate inside oxidized domains, given the weaker behavior of oxidized regions according to

DFTB calculations. However, it is remarkable that the first observation of damage localization in FEA and MD simulations occur in the same oxidized domain for the simulated GO membrane. This can be explained based on the nature of the patchy structure, in which the initiation of crack is related to two factors. The first one is the geometric oxidation pattern, reflected in the shape of the oxidized islands, which determines stress concentration and damage accumulation on the monolayer (shown in Fig. 12b). The second factor is the distribution of two different types of functional groups within the oxidized domain. Due to the random generation of the two types in the oxidized domains, there could be differences in the crack initiation sites. In this respect, we note that in 39, out of the 40 investigated RVEs, the crack initiated at the same location within the band of oxidized elements. In the current comparison, the existence of a relatively narrow region of oxidized elements, similar to necking within island-like domains, exists in both FEA and MD models and leads to localization, directing crack propagation through the oxidized regions. Consequently, it is reasonable to expect consistent localization in different tests on the same morphology, irrespective of the local details of oxidation simulated in MD given that such regions are generally weaker than graphene. Notably, despite the location where localization occurs, tests on different larger monolayers produce consistent stress–strain response, which will be discussed in the next section. After micro-damage coalesces at a macro-strain level of ∼7%, a crack starts to localize in FEM and MD calculations. For the MD simulations, Fig. 11 shows the initial softening preceding the large drop in stress leading to failure of the entire monolayer. In addition, this figure also shows that MD can sustain more (about 20%) strain before catastrophic failure as compared to our continuum model. This can be explained by: (1) the further transformation of covalent bonds which endows GO with slightly higher failure strain (Soler-Crespo et al., 2016) and (2) the wrinkling (out-of-plane) deformation at the near-tip region, triggering mode mixity during crack growth (Zhang et al., 2014). These phenomena seemingly delay the propagation of the crack and allow more energy dissipation. However, the good agreement between FEM and MD, with respect to the elastic and fracture features, confirms the validity of the FE model in predicting the behavior of GO membranes where the island-like microstructure is considered, and enables us to explore length scales at which an RVE for GO can be established.

5. Simulation of GO membranes under uniaxial and biaxial strain loading

Several sets of functionalized membranes were generated using the procedure discussed in Section 2.1, and analyzed using the FEA framework developed in Sections 2 and 3. Each analysis set $S_{C\%}^M$ consists of M different 40×40 nm^2 GO membranes, with a randomly generated microstructure, where the percentage of area coverage of the oxidized regions is given by $C\%$. We set $M = 40$ and use these GO membranes to investigate the role of microstructure in the mechanical behavior of GO; in particular, six different sets have been generated with $C\% \in [0, 20, 40, 60, 80, 100]$. Subsequently, for each of the M generated membranes, 20×20 nm^2 regions of each membrane were extracted to investigate the effect of membrane size on mechanical response, and assess the critical dimension at which the existence of a representative behavior can be identified. Thus, in summary, for each set $S_{C\%}^M$ containing M morphologies with a $C\%$ percent oxidized area, two $S_{C\%}^{M,L}$ square membranes are extracted with dimension $L = [20, 40]$ nm and subjected to FEA analysis. Each membrane in the $S_{C\%}^{M,L}$ sets is subjected to uniaxial macro-strains $\boldsymbol{\eta_{uni}}$ along the armchair (x_1) and zigzag (x_2) directions of the graphitic backbone, and to equibiaxial macro-strains $\boldsymbol{\eta_{bi}}$. In our calculations, progressive strain loading is applied up to membrane failure. The apparent macro-stress components are computed by homogenizing the micro-stress over the volume of each membrane, and results are reported in GPa.

Fig. 13 shows contour plots of variables of interest from the FE analysis of a 40×40 nm^2 epoxide-rich GO membrane with a 60% oxidation level, i.e., $C\% = 60\%$. The microstructure and failure pattern is shown in Fig. 13a, and the damage pattern before failure (Fig. 13b), as well as micro-strain (Fig. 13c) and micro-stress (Fig. 13d) fields at $\varepsilon_{ac} = 7.75\%$, are shown for clarity. Interestingly, in our calculation, we observe that the crack path initiates and attempts to follow a path along weaker oxidized domains. Fig. 14 further shows computed macro-stress *versus* macro-strain curves for the membranes belonging to the $S_{60\%}^{40,L}$ set with varying dimension L (where $L =$ nm), i.e., $S_{60\%}^{40,20}$ and $S_{60\%}^{40,40}$. To account for statistics regarding failure macro-strain in each plot, three vertical dashed lines identify, from left to right, the minimum, average, and maximum macro-strains corresponding to the interval $[\bar{\eta}_f - 2\sigma, \bar{\eta}_f + 2\sigma]$, where $\bar{\eta}_f$ and σ represent the average and standard deviation metrics for failure strains, respectively; within this region 95.5% of the specimens will undergo failure for a normal distribution of failure strains.

A common feature among the tests is the sudden failure of specimens, as captured by the obtained macro stress-strain curves. In comparison with epoxide-rich GO monolayers of the same size, hydroxyl–rich GO specimens converge to a representative response for smaller specimen lengths L, despite the distribution of oxidized regions. From the obtained results, it is reasonable to claim that 40×40 nm^2 GO membranes exhibit a representative mechanical behavior and identify a critical length scale in terms of GO's microstructure. This conclusion should not only hold for the morphologies generated by the proposed random method. Indeed, the structure generation framework proposed herein can also be used to extract the mechanical behavior of GO monolayers imaged in TEM, or to assess the role of synthesis in the resultant properties of the material.

Up to this point, the specimen length $L = 40$ nm has been shown to produce convergent results, independent of morphologies. Therefore, this specimen length will be used further to investigate the relationship between oxidized area percentage and macro stress-strain in GO, which is captured in Fig. 15. Each plot corresponds to a specific loading condition, while each curve in the plots is a macro stress-strain response of membranes with different oxidation area coverage $C\%$, of dimension 40×40 nm^2; in others words, the plots in Fig. 15 collect the data for all considered oxidation levels. The failure

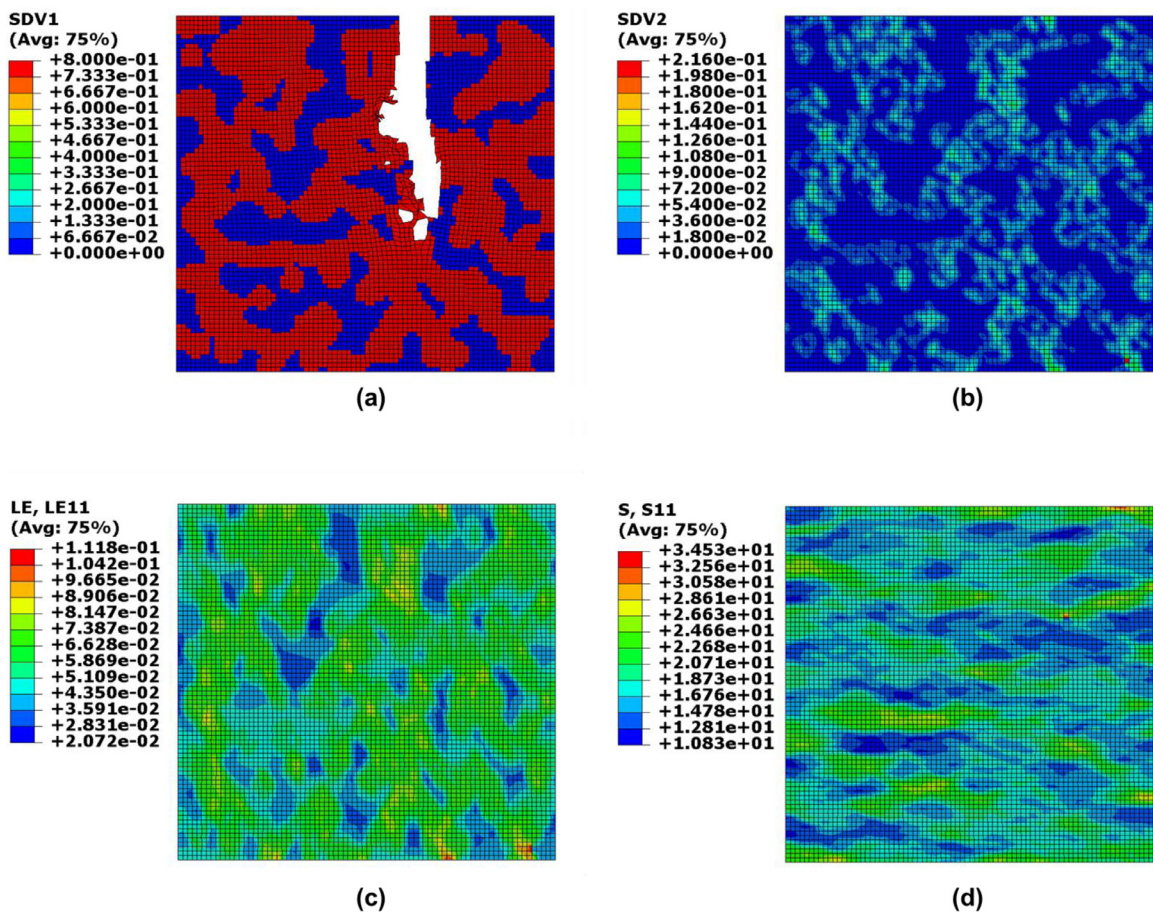**Fig. 13.** Finite element patterns for a 40×40 nm^2 epoxide-rich GO membrane with 60% oxidation level subjected to uniaxial strain tension along the x$_1$ (armchair) direction. Shown are the (a) FE mesh, oxidation and failure patterns (red regions represent oxidized domains), (b) damage pattern immediately before failure, $\varepsilon_{ac} = 8.67\%$ (c) logarithmic micro-strain field ε_{ac}^{ac} at $\varepsilon_{ac} = 7.75\%$ and, d) Cauchy micro-stress field σ_{ac}^{ac} at $\varepsilon_{ac} = 7.75\%$. (For interpretation of the references to color in this figure legend, the reader is referred to the web version of this article.)

strain of each curve is arrested at the average failure macro-strain. We observe that the mechanical behavior of GO membranes depends heavily on oxidation percentage, which plays a role analogous to the volume fraction V_f in heterogeneous composites, and is in agreement with previous findings on the local behavior of GO nano-flakes (Soler-Crespo et al., 2016). Specifically, we observe that homogeneous specimens (*i.e.,* 0% and 100% coverage levels) sustain higher strains to failure due to the lack of heterogeneities, which act as significant stress concentration regions, when graphitic and oxidized domains are adjoined. At low oxidations levels, where oxidized regions behave similarly to defects, the brittle nature of graphene makes it sensitive to the presence of such stress concentrations. This will give it lower strains to failure, as captured in our simulations, and the effect of this behavior should reduce as the material becomes more oxidized.

Notably, the material does not behave isotropically under uniaxial tensile strain, as different average failure macro-strains are obtained from uniaxial strain loading along the zigzag and armchair directions. This anisotropy is more pronounced for low oxidation levels, for which graphitic regions become more prevalent and the anisotropy of graphene contributes significantly to overall material behavior. Importantly, these obtained RVE results and structure-property relationships can be used, after validation with other methods, towards the design of GO based nanocomposites and to access significantly larger length scales in the study of GO-based systems.

The relationship between chemical composition and the mechanical behavior of GO monolayers has been previously investigated in DFTB with 2×2 nm^2 GO monolayers (Meng et al., 2017; Soler-Crespo et al., 2016), and a brittle to quasi-brittle transition was identified as GO became epoxide-rich. However, it was not revealed if such a transition, which increases strain to failure at the nanoscale, will persist at larger scales where the island-like microstructure of GO is prevalent and leads to different failure behavior. Fig. 16 shows the average stress-strain curves extracted from ten 40×40 nm^2 GO monolayers. The probed monolayers all have an oxidation level of 60%, but different epoxide-to–hydroxyl functional group ratios, represented by the parameter $\delta = A_{epoxide}/(A_{epoxide} + A_{hydroxyl})$, where A_i represents the area of the ith phase. At this larger length scale we still observe a brittle to quasi-brittle transition as the value of δ ranges from zero to one, evident from the increase in failure
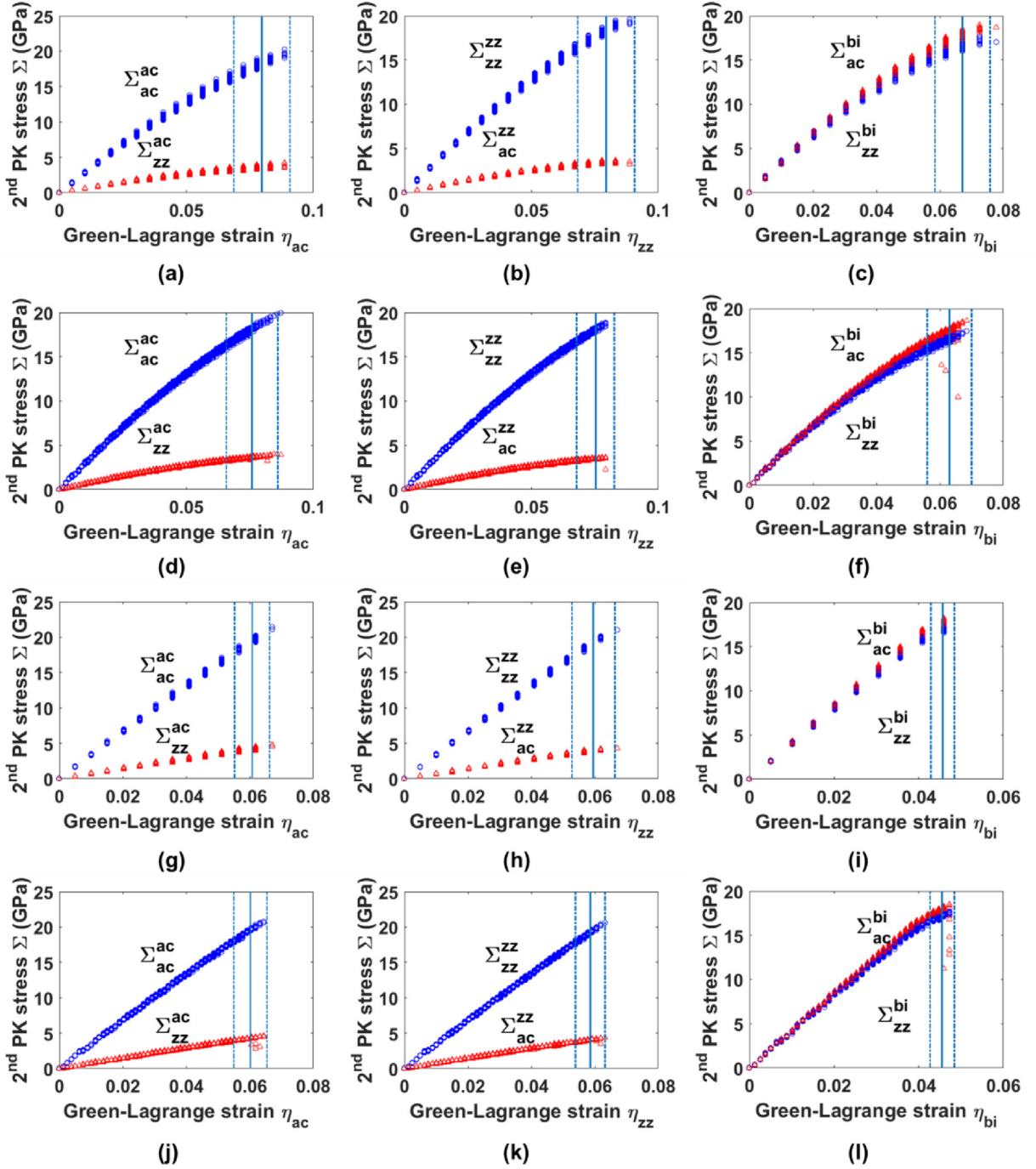
Fig. 14. (a–f) Macro stress-strain curves for 60% oxidized, epoxide-rich (a–c) 20×20 nm^2 and (d–f) 40×40 nm^2 GO membranes. (g–l) Macro stress-strain curves for 60% oxidized, hydroxyl–rich (g–i) 20×20 nm^2 and (j–l) 40×40 nm^2 GO membranes. Here, the first, second and third columns correspond to uniaxial tensile strain along the armchair and zigzag directions, and equibiaxial tensile strain, respectively.

strain from $6 + 0.32\%$ to $8 + 0.54\%$. However, the phenomena at this scale is not as pronounced as in the nanoscale based on DFTB simulations. We believe this observation is due to the fact that the graphitic backbone is brittle and sensitive to the presence of material heterogeneities, which dominates energy release during fracture. In particular, the concentration of oxidation regions into island-like "patches" creates stress concentration regions that adjoin graphitic domains. In this light, it is unsurprising that the accumulation of energy dissipating epoxide-rich domains is unable to balance the brittle fracture and drastic release of energy from graphitic regions, which leads to sudden failure of GO specimens.
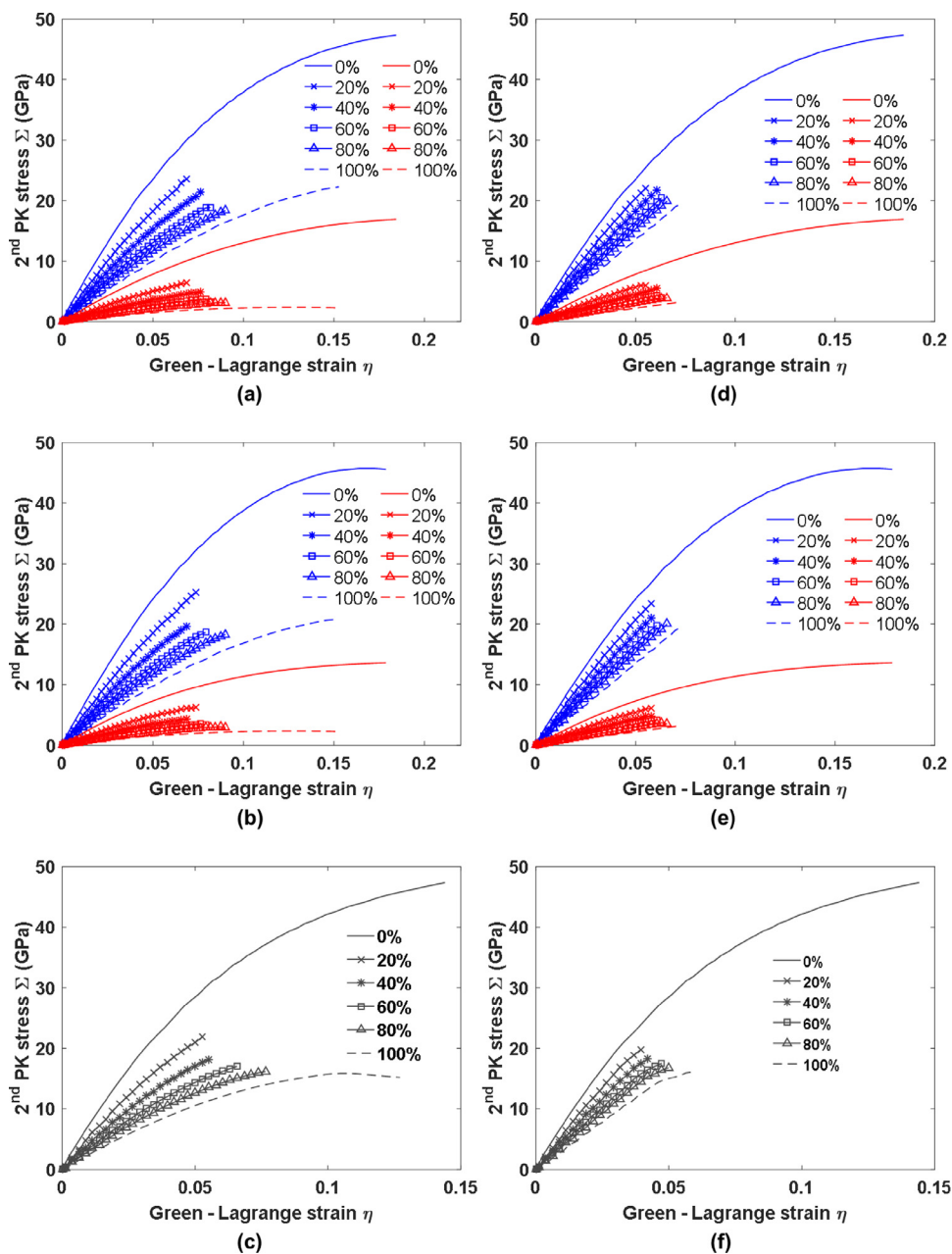
Fig. 15. Macro stress-strain trends for different overall oxidation ratios. (a-c) Macro stress-strain behavior for epoxide-rich GO with varying oxidation level subject to uniaxial tensile strain along the (a) armchair and (b) zigzag directions, or (c) equibiaxial tensile strain. (d-f) Macro stress-strain behavior for hydroxyl–rich GO with varying oxidation level subject to uniaxial tensile strain along the (d) armchair and (e) zigzag directions, or (f) equibiaxial tensile strain. For uniaxial tensile strain curves, blue and red lines represent Σ_x^x and Σ_y^x, respectively. (For interpretation of the references to color in this figure legend, the reader is referred to the web version of this article.)

6. Effect of defects on GO monolayer behavior

It is worth mentioning that, a stochastic distribution of initial damage within the oxidized areas should also be considered as the synthesis route of graphene and GO possibly generates inevitable topological defects (*e.g.*, voids or minor cracks) within the material, which influence mechanical behavior and fracture. Graphene, according to previous reports (Zandiatashbar et al., 2014), is sensitive to defects as its effective strength heavily depends on the presence of damage and defects in its microstructure. Hydroxyl-rich GO, in which the presence of –OH groups significantly lower the intrinsic strength of the C–C bonds in its hexagonal rings, has also been demonstrated to be brittle and sensitive to defects. However, the presence of epoxide functional groups will arrest the propagation of micro-damage, leading to higher energy dissipation
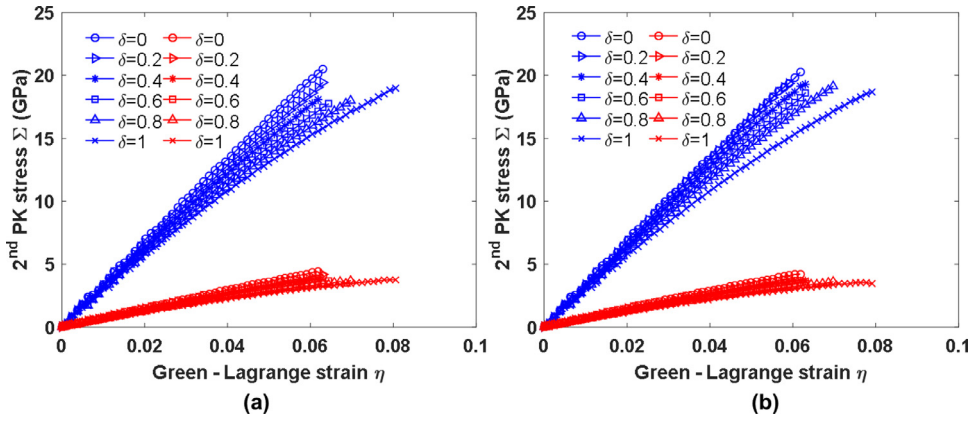
Fig. 16. Transition in brittle to quasi-brittle behavior of 60% oxidized GO based on observed macro stress-strain behavior under uniaxial strain tension along the (a) armchair and (b) zigzag directions, for varying GO chemical composition, δ. Blue and red lines represent Σ_x^x and Σ_y^x, respectively. (For interpretation of the references to color in this figure legend, the reader is referred to the web version of this article.)
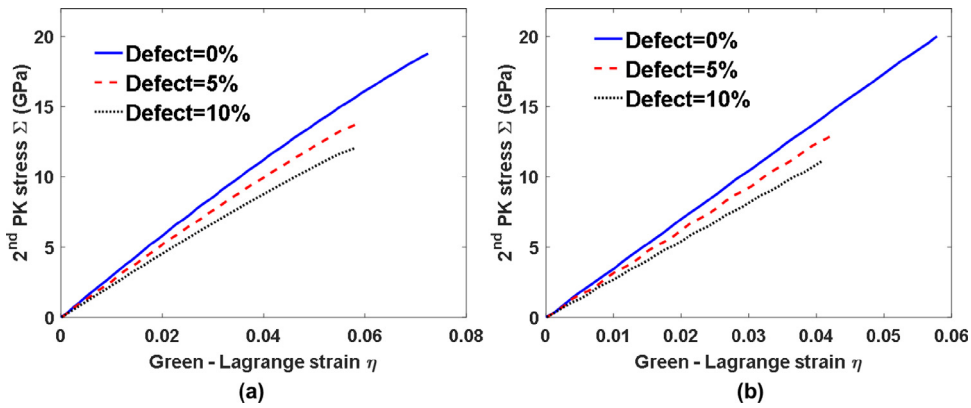

Fig. 17. Effect of randomly generated defects on the macro stress-train behavior of 40×40 nm^2 GO monolayers with a 60% oxidation level subjected to uniaxial tensile strain along the armchair direction for (a) epoxide-rich and (b) hydroxyl–rich compositions.

before macro damage is observed (Soler-Crespo et al., 2016). Therefore, given its quasi-brittle behavior, it is reasonable to expect that epoxide-rich GO is less sensitive to defects.

To investigate the effect of pre-existing voids on GO with different chemical composition, 40×40 nm^2 GO monolayers were subjected to uniaxial tensile strain along the armchair direction. A quantitative estimate of this initial damage pattern, provided as additional inputs to the FEA, would require a careful investigation aiming at correlating such pattern with real microstructures. However, in order to understand how defects affect GO monolayers' behaviors, locations for voids were generated randomly within oxidized domains, and their constitutive behavior was implemented by setting the damage variable $d = 0.99$ for elements representing voids. Due to the irreversible nature of the damage in our model, these elements lose their stiffness almost entirely. Fig. 17 shows the macro stress-strain behavior of two GO monolayers with the same oxidation level but different chemical composition. When 5% of the elements on the monolayer are damaged, the nominal strength of hydroxyl–rich GO decreases by 35%, whereas the nominal strength for epoxide-rich GO decreases only by 25%. By investigating the stress distribution of regions around the crack tip, we observe that the fracture process zone is slightly larger for epoxide-rich GO compositions. However, both GO chemistries exhibit behavior that is similar to crack propagation predicted by linear elastic fracture mechanics, which agrees well with the behavior reported for GO modeled with the coarse – grained molecular dynamics approach (Meng et al., 2017). Indeed, the trends captured in our FEM model confirm that the quasi-brittle behavior of epoxide-rich domains is less sensitive to defects.

7. Simulation of membrane deflection using FEM model

Although experimental uniaxial and equibiaxial tensile tests of GO membranes are useful to extract information about the material behavior, they are extremely difficult to conduct. Thus, membrane deflection experiments with an atomic force microscope, which is a less direct measurement but still reasonably indicative of mechanistic behavior, are often utilized to extract the mechanical behavior of 2D materials, such as GO. Particularly, such a measurement is useful to determine material stiffness, and has been recently utilized to detect energy dissipation due to damage (Wei et al., 2015). To demon-
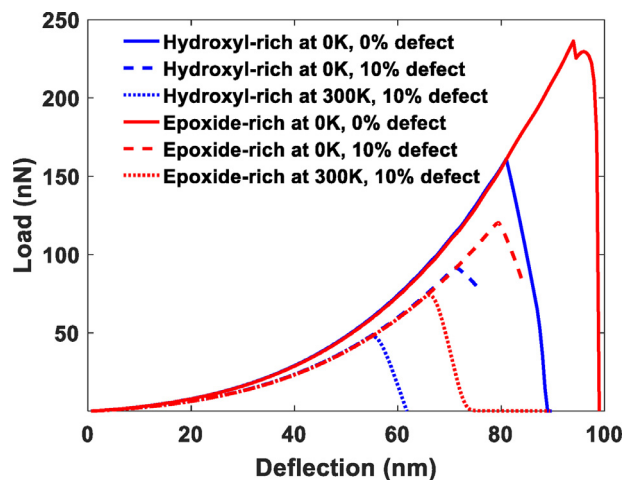
Fig. 18. Load -deflection results for defective and pristine GO membranes with varying chemical composition.

strate the applicability of our model, we simulated membrane deflection experiments for hydroxyl–rich and epoxide-rich GO membranes, with and without defects, to predict the behavior of different types of GO subjected to membrane deflection experiments.

The membrane deflection test is simulated using membrane elements of size 0.5 nm. The membrane radius is 1860 nm while the tip radius is 25 nm, and their contact is implemented using hard normal and frictionless tangential behavior. The velocity of the indenter is 1 μm/s, which is slow enough to consider the process quasi-static. Fig. 18 compares the load-deflection curves for a number of cases where parameters are calibrated based on DFTB results at 0 K (molecular mechanics) and at 300 K (based on DFTB-trained Car-Parrinello molecular dynamics). Moreover, defects are implemented into the membrane, using the approach described in Section 6, to inversely predict the amount of pre-existing damage in previously reported experimental measurements. In Fig. 18, all of the curves follow the relation (Lee et al., 2008):

$$F = \sigma_0 \pi t_0 \delta + \frac{Et_0}{q^3 a^2} \delta^3 \tag{18}$$

where F is the applied force, σ_0 is the pre-stress in the membrane, $t_0 = 0.75$ nm is the membrane's thickness, $a = 1860$ nm is the radius of the membrane, q is a dimensionless parameter computed from GO Poisson's ratio, and δ is the membrane's deflection. The tip radius is 25 nm as mentioned earlier. At higher temperature, due to the influence of thermal energy in lowering energy barriers, the macro stress- strain behavior is reduced as reported by Espinosa and co-workers (Wei et al., 2015), which results in lower peak loads. Furthermore, when defects are introduced into GO monolayers, both peak load and stiffness are reduced. From the examined cases, those that exhibited the lowest peak load correspond to the behavior of GO at 300 K with 10% defect density. Herein, it should be noted that the effect of temperature is implicitly considered within the parametric calibration using DFTB results, where athermal and room temperature behavior were separately considered. Temperature effects on the mechanical behavior of 2D materials were discussed in previous studies for graphene (Gao and Huang, 2014) and may be introduced to FE model by adding thermal-related terms in the constitutive law; however, this aspect is not directly covered by the current study. Remarkably, these results match well with previously reported experimental findings (Wei et al., 2015). Our results suggest that even though hydroxyl– and epoxide-rich chemistries have similar strength values, the peak load of epoxide-rich chemistries is higher. This is presumably due to micro-damage evolution and localization response of epoxide-rich GO monolayers, which have been shown to allow more energy dissipation, and therefore can sustain higher deflections and loads.

To further explore this hypothesis, we studied the rupture process of the membranes during the FEM simulations. Fig. 19c provides insight as to how the membranes respond to changes in displacement of the AFM tip, which is controlled during both simulations and experiments. In snapshots I and II, which correspond to hydroxyl–rich GO chemistry, macro-cracks start to nucleate, and the membrane is immediately punctured. Prior to this point, there is no energy dissipation mechanism, and so the elastic energy stored in the body is released abruptly, leading to unstable crack propagation. The size of the hole on the membrane for this case exceeds the diameter of the tip due to the unstable growth of cracks. On the contrary, for snapshots III-VI, which correspond to the epoxide-rich GO case, micro-damage can be accumulated and energy can be dissipated through the quasi-brittle behavior of epoxide-rich domains prior to the coalescence of micro cracks. In particular, for snapshots IV to V, the element experiencing the maximum strain on the membrane is damaged, but the membrane is able to continue bearing load and does not rupture. The accumulation of micro-damage continues as the AFM tip is further displaced into the membrane, leading to the accumulation of damage in adjacent elements, until a critical damage level is achieved for a particular set of elements. At this point, the membrane cannot bear further stress, cracks nucleate and propagate, and the membrane ruptures. However, in this case, because a significant amount of energy has been previously
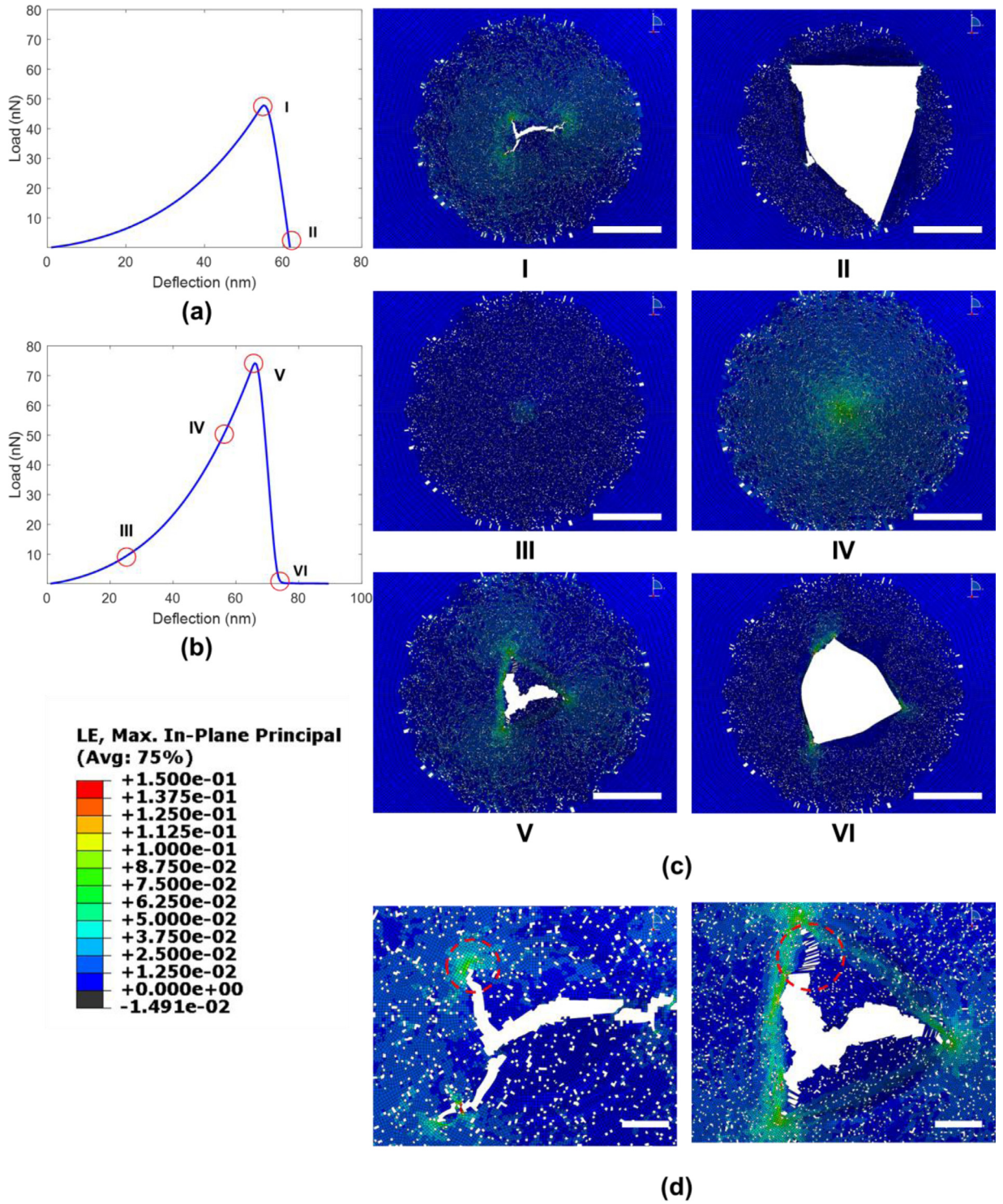
Fig. 19. Load-deflection curve for (a) hydroxyl–rich GO and (b) and epoxide-rich GO at 300 K and 10% defect density. (c) Snapshots corresponding to points on the load-displacement curves shown in (a-b) (scale bar: 50 nm). (d) Fracture process zone in hydroxyl GO and epoxide GO (scale bar: 10 nm). The contours in (c) and (d) represent in-plane principal strain distribution corresponding to the color bar shown within.

dissipated, the crack grows in a stable fashion, and stops propagating when the rupture diameter approximates the diameter of the AFM tip ($\sim$50 nm). A similar phenomenon was reported by Espinosa and co-workers (Wei et al., 2015) for membrane deflection experiments with 70% oxidized, epoxide-rich GO. Clearly, our FEM results predict that the fabrication process utilized in this literature led to a likely defect density of approximately 10%. A close inspection of the fracture process zone (Fig. 19d) for both GO chemistries closely agrees with the analysis of Fig. 19c.

8. Conclusion

In this study, we derived an energy-consistent continuum model that predicts the response of GO monolayers consisting of graphitic and oxidized domains subjected to tension. The model is based on DFTB constitutive response of the two phases. Using MD simulations, the developed framework was validated and utilized to predict the existence of GO RVEs. Interestingly, the simulations show that prior to achieving peak stress, the stress-strain behavior of 40×40 nm^2 GO membranes, with various distributions of oxidation patches, converge to an RVE response independently of such distribution. We conclude that this response can be used to simulate GO at larger scales, without characterizing exactly the patchy nature. Also, the larger scale GO specimens maintain mechanical specificity based on the oxidation level and chemical composition of the material, providing tunability at the microscale. In addition, we explored the role of defect density in GO, and validated the applicability of the model to larger length scales by predicting membrane deflection behavior, in close agreement with previous experimental and theoretical observations. The results of this study establish a theoretical and predictive framework, which is directly applicable in the study of macroscopic GO-based structures and that can expedite materials and device design efforts. One approach that can extend the presented analysis is the design of multilayered configurations, where the estimation of the mutual interactions between various regions (graphic and oxidized) of different layers play a major role. This, in turn, requires accurate formulations of interfacial laws (*e.g.,* interfacial cohesion and shear) based on focused atomistic investigations after force field validation. The more complex mixed interactions between graphitic and oxidized regions in a random arrangement is left for future investigation. Therefore, we anticipate that the results of this study will become a crucial step toward the development of reduced order models for 2D materials exhibiting patchy structures, and pave the way for FEM-guided design of advanced engineering materials.

Appendix A. Calculation of crack band theory parameters

Upon introduction of the crack band model, the constitutive behavior for graphene introduced in Eq. (2) is supplemented with a strain softening behavior and can be rewritten as

$$\Sigma_i^{Gr} = (1 - d)\left(C_{ij}\eta_j + \frac{1}{2!}C_{ijk}\eta_j\eta_k + \frac{1}{3!}C_{ijkl}\eta_j\eta_k\eta_l\right) \tag{A.1}$$

where $d = d[\xi(\boldsymbol{\eta})] \in [0, 1]$ is defined as

$$d[\xi(\boldsymbol{\eta})] = \frac{\langle \xi^* - 1 \rangle}{\xi_f(h_e) - 1} \; and \; \xi^* = \max_{loading\ history}[\xi(\boldsymbol{\eta})] \in \left[1, \; \xi_f\right] \tag{A.2}$$

Here, ξ is defined by Eq. (3). The parameter $\xi_f(h_e)$ in the previous equation must be determined, for each finite element, on the basis of its characteristic length h_e, after assessing that the condition $h_e \leq h_e^*$ is satisfied. To achieve this, the critical length size h_e^* is first determined by considering a uniaxial strain condition and solving the following equation in the armchair direction (with $\theta = 0$)

$$\int_0^{\bar{\eta}_{ac}} \Sigma_1^{Gr}(\eta_1)d\eta_1 = \frac{G_{Gr}}{h_e^*} \tag{A.3}$$

where $\eta_1 \equiv \eta_{ac}$, G_{Gr} is the critical energy release rate of graphene (Zhang et al., 2014) normalized by t_0, which is the assumed membrane thickness ($t_0 = 0.75$ nm in this work). By selecting an element size $h_e < h_e^*$, the value $\xi_f(h_e)$ to be inserted in Eq.

(A.2) is computed by solving the equation

$$\int_{\bar{\eta}_{ac}}^{\bar{\eta}_{ac}\xi_f} \Sigma_1^{Gr}(\eta_1)d\eta_1 = \frac{G_{Gr}}{h_e} - \int_0^{\bar{\eta}_{ac}} \Sigma_1^{Gr}(\eta_1)d\eta_1 \tag{A.4}$$

Given the expressions used in Eqs. (A.1) and (A.2), (A.4) can be solved analytically. In this work, the critical energy release rate of graphene, $G_{Gr} = 7.21\,\text{J m}^{-2}$, is used. This energy release rate corresponds to the values reported elsewhere (Zhang et al., 2014) when it is scaled to account for thickness differences between graphene and GO ($G = 16\,\text{J/m}^2$ at $t_0 = 0.34\,\text{nm}$, which leads to $G = 7.21\,\text{J/m}^2$ at GO's thickness). Using the constitutive laws developed for pristine graphene, *i.e.,* graphitic regions, a critical element size $h_{graphitic}^* = 0.78\,\text{nm}$ is determined.

As previously defined in the thermodynamically consistent framework for oxidized regions, the energy dissipated by damage can be calculated by

$$W^d = \int_0^1 Y(d, \boldsymbol{\eta})\Delta d \tag{A.5}$$

Then, the critical element size is found by calculating the dissipated energy

$$\int_0^1 Y(d, \boldsymbol{\eta}, \beta_1)\Delta d = \frac{G_{GO}}{h_e^*} \tag{A.6}$$

where G_{GO} is the critical energy release rate of GO, β_1 is the value of β where the stress – strain curve starts to manifest the snap-back. Due to the definition given by Eq. (13), β can be varied to tune the softening response so the fracture energy is kept constant during the damage process, independently of the size of the element. β is calculated numerically by solving the following equation:

$$\int_0^1 Y(d, \boldsymbol{\eta}, \beta)\Delta d = \frac{G_{GO}}{h_e} \tag{A.7}$$

Previously, the critical energy release rate for epoxide-rich and hydroxyl–rich GO monolayers was calculated based on Griffith criterion calculations using coarse-grained molecular dynamics (CG-MD) simulations. Herein, we also estimated the energy release rate by the product of the average value of the area under the stress-strain curves in DFTB and the characteristic element length, which is 2 nm. Although the obtained value for epoxide-rich GO agrees well between both methods ($G_{epoxide} \approx 6.11\,\text{J m}^{-2}$), there is a variation for the energy release rate of hydroxyl–rich GO ($G_{hydroxyl} \approx 2.5\,\text{J m}^{-2}$ for the DFTB approach *vs* $G_{hydroxyl} \approx 4.5\,\text{J m}^{-2}$ using CG-MD). Therefore, we utilized the lower value ($G_{hydroxyl} \approx 2.5\,\text{J m}^{-2}$) to ensure the toughness of hydroxyl–rich GO structures was not overestimated. Furthermore, the utilized value is a reasonable given recent estimates of GO's energy release rate in the literature (Meng et al., 2017). In the end, we obtained critical element sizes $h_{epoxide}^* = 3.20\,\text{nm}$ and $h_{hydroxyl}^* = 2.01\,\text{nm}$ for our simulations based on the previously discussed approach.

References

Abaqus, V., 2014. 6.14 Documentation.

Bažant, Z.P., Oh, B.H., 1983. Crack band theory for fracture of concrete. Matér. Constr. 16, 155–177.

Bazant, Z.P., Planas, J., 1997. Fracture and Size Effect in Concrete and Other Quasibrittle Materials. CRC press.

Beese, A.M., An, Z., Sarkar, S., Nathamgari, S.S.P., Espinosa, H.D., Nguyen, S.T., 2014. Defect-tolerant nanocomposites through bio-inspired stiffness modulation. Adv. Funct. Mater. 24, 2883–2891.

Cao, C., Daly, M., Singh, C.V., Sun, Y., Filleter, T., 2015. High strength measurement of monolayer graphene oxide. Carbon 81, 497–504.

Chenoweth, K., Van Duin, A.C., Goddard, W.A., 2008. ReaxFF reactive force field for molecular dynamics simulations of hydrocarbon oxidation. J. Phys. Chem. A 112, 1040–1053.

Compton, O.C., Cranford, S.W., Putz, K.W., An, Z., Brinson, L.C., Buehler, M.J., Nguyen, S.T., 2012. Tuning the mechanical properties of graphene oxide paper and its associated polymer nanocomposites by controlling cooperative intersheet hydrogen bonding. ACS Nano 6, 2008–2019.

Dreyer, D.R., Park, S., Bielawski, C.W., Ruoff, R.S., 2010. The chemistry of graphene oxide. Chem. Soc. Rev. 39, 228–240.

Dua, V., Surwade, S.P., Ammu, S., Agnihotra, S.R., Jain, S., Roberts, K.E., Park, S., Ruoff, R.S., Manohar, S.K., 2010. All-organic vapor sensor using inkjet-printed reduced graphene oxide. Angew. Chem. Int. Ed. 49, 2154–2157.

Erickson, K., Erni, R., Lee, Z., Alem, N., Gannett, W., Zettl, A., 2010. Determination of the local chemical structure of graphene oxide and reduced graphene oxide. Adv. Mater. 22, 4467–4472.

Feder, J., 1980. Random sequential adsorption. J. Theor. Biol. 87, 237–254.

Gao, W., Huang, R., 2014. Thermomechanics of monolayer graphene: rippling, thermal expansion and elasticity. J. Mech. Phys. Solids 66, 42–58.

Hanson, M.A., 1981. On sufficiency of the Kuhn-Tucker conditions. J. Math. Anal. Appl. 80, 545–550.

Jang, J.H., Woo, J.Y., Lee, J., Han, C.-S., 2015. Ultrathin graphene oxide membranes for water purification. In: Nanotechnology (IEEE-NANO), 2015 IEEE 15th International Conference on. IEEE, pp. 212–215.

Jhon, Y.I., Chung, P.S., Smith, R. & Jhon, M.S. 2012. Molecular simulation of fracture dynamics of symmetric tilt grain boundaries in graphene. *arXiv preprint* arXiv:1202.2613.

Kachanov, L., Krajcinovic, D., 1987. Introduction to continuum damage mechanics. J. Appl. Mech. 54, 481.

Kuila, T., Mishra, A.K., Khanra, P., Kim, N.H., Lee, J.H., 2013. Recent advances in the efficient reduction of graphene oxide and its application as energy storage electrode materials. Nanoscale 5, 52–71.

Lee, C., Wei, X., Kysar, J.W., Hone, J., 2008. Measurement of the elastic properties and intrinsic strength of monolayer graphene. Science 321, 385–388.

Lu, Q., Huang, R., 2009. Nonlinear mechanics of single-atomic-layer graphene sheets. Int. J. Appl. Mech. 1, 443–467.

Marianetti, C.A., Yevick, H.G., 2010. Failure mechanisms of graphene under tension. Phys. Rev. Lett. 105, 245502.

Medhekar, N.V., Ramasubramaniam, A., Ruoff, R.S., Shenoy, V.B., 2010. Hydrogen bond networks in graphene oxide composite paper: structure and mechanical properties. Acs Nano 4, 2300–2306.

Melro, A., Camanho, P., Pires, F.A., Pinho, S., 2013. Micromechanical analysis of polymer composites reinforced by unidirectional fibres: Part I–Constitutive modelling. Int. J. Solids Struct. 50, 1897–1905.

Meng, Z., Soler-Crespo, R.A., Xia, W., Gao, W., Ruiz, L., Espinosa, H.D., Keten, S., 2017. A coarse-grained model for the mechanical behavior of graphene oxide. Carbon 117, 476–487.

Paci, J.T., Belytschko, T., Schatz, G.C., 2007. Computational studies of the structure, behavior upon heating, and mechanical properties of graphite oxide. J. Phys. Chem. C 111, 18099–18111.

Pijaudier-Cabot, G., Bažant, Z.P., 1987. Nonlocal damage theory. J. Eng. Mech. 113, 1512–1533.

Rezania, B., Severin, N., Talyzin, A.V., Rabe, J.R.P., 2014. Hydration of bilayered graphene oxide. Nano Lett. 14, 3993–3998.

Robinson, J.T., Perkins, F.K., Snow, E.S., Wei, Z., Sheehan, P.E., 2008. Reduced graphene oxide molecular sensors. Nano Lett. 8, 3137–3140.

Ryoo, S.-R., Lee, J., Yeo, J., Na, H.-K., Kim, Y.-K., Jang, H., Lee, J.H., Han, S.W., Lee, Y., Kim, V.N., 2013. Quantitative and multiplexed microRNA sensing in living cells based on peptide nucleic acid and nano graphene oxide (PANGO). ACS Nano 7, 5882–5891.

Soler-Crespo, R.A., Gao, W., Xiao, P., Wei, X., Paci, J.T., Henkelman, G., Espinosa, H.D., 2016. Engineering the mechanical properties of monolayer graphene oxide at the atomic level. J. Phys. Chem. Lett. 7, 2702–2707.

Van Duin, A.C., Dasgupta, S., Lorant, F., Goddard, W.A., 2001. ReaxFF: a reactive force field for hydrocarbons. J. Phys. Chem. A 105, 9396–9409.

Wan, J., Jiang, J.-W., Park, H.S., 2017. Negative Poisson's ratio in graphene oxide. Nanoscale 9, 4007–4012.

Wei, X., Fragneaud, B., Marianetti, C.A., Kysar, J.W., 2009. Nonlinear elastic behavior of graphene: ab initio calculations to continuum description. Phys. Rev. B 80, 205407.

Wei, X., Kysar, J.W., 2012. Experimental validation of multiscale modeling of indentation of suspended circular graphene membranes. Int. J. Solids Struct. 49, 3201–3209.

Wei, X., Mao, L., Soler-Crespo, R.A., Paci, J.T., Huang, J., Nguyen, S.T., Espinosa, H.D., 2015. Plasticity and ductility in graphene oxide through a mechanochemically induced damage tolerance mechanism. Nat. Commun. 6.

Xu, J., Wang, K., Zu, S.-Z., Han, B.-H., Wei, Z., 2010. Hierarchical nanocomposites of polyaniline nanowire arrays on graphene oxide sheets with synergistic effect for energy storage. ACS Nano 4, 5019–5026.

Xu, M., Paci, J.T., Oswald, J., Belytschko, T., 2012. A constitutive equation for graphene based on density functional theory. Int. J. Solids Struct. 49, 2582–2589.

Xu, Y., Hong, W., Bai, H., Li, C., Shi, G., 2009. Strong and ductile poly (vinyl alcohol)/graphene oxide composite films with a layered structure. Carbon 47, 3538–3543.

Zandiatashbar, A., Lee, G.-H., An, S.J., Lee, S., Mathew, N., Terrones, M., Hayashi, T., Picu, C.R., Hone, J., Koratkar, N., 2014. Effect of defects on the intrinsic strength and stiffness of graphene. Nat. Commun. 5, 3186.

Zhang, P., Ma, L., Fan, F., Zeng, Z., Peng, C., Loya, P.E., Liu, Z., Gong, Y., Zhang, J., Zhang, X., 2014. Fracture toughness of graphene. Nat. Commun. 5.